



POLITECNICO
MILANO 1863

RE.PUBLIC@POLIMI

Research Publications at Politecnico di Milano

Post-Print

This is the accepted version of:

D. Prederi, A. Parrinello, A. Gadda, P. Mantegazza
Flutter Analysis of Propfan-Open Rotors
Journal of Aircraft, Vol. 55, N. 3, 2018, p. 1024-1040
doi:10.2514/1.C034468

The final publication is available at <https://doi.org/10.2514/1.C034468>

Access to the published version may require subscription.

When citing this work, cite the original published paper.

Permanent link to this version

<http://hdl.handle.net/11311/1063038>

Flutter Analysis of Propfan-Open Rotors

Davide Prederi*

Leonardo Helicopters, Cascina Costa di Samarate, Varese, Italy.

Andrea Parrinello[†], Andrea Gadda[‡] and Paolo Mantegazza[§]

Department of Aerospace Sciences and Technologies, Politecnico di Milano, Milano, Italy

The work aims at showing the importance of flutter predictions in the preliminary design of Propfan-Open Rotors. Both single rotating propellers and contra rotating open rotors are investigated. The related structural sub-systems are modelled through finite element analyses, the aerodynamic sub-systems exploit a finite volume full potential formulation suitable for unsteady transonic flows. An *ad hoc* technique is developed for simulating the flow field around a contra rotating open rotor configuration. The effectiveness of the proposed aeroelastic analysis is successfully assessed for single propellers through comparisons with reference numerical and experimental data available in the literature, as well as against Euler flow based solutions. Results for contra rotating open rotors cannot be validated because of the lack of corresponding open literature data.

Key words: aeroelasticity, contra-rotating open rotor, transonic flow, flutter, full potential.

Nomenclature

N_b	Number of Blades
ρ	density
p	Pressure
c_∞	asymptotic sound speed
M_∞	Asymptotic Mach number
\mathbf{R}	Position of a fluid volume
\mathbf{u}	Absolute Velocity

*Leonardo Helicopters, Rotor Dynamics and Loads Analyst, Cascina Costa di Samarate, Varese, Italy.

[†]Ph.D., Department of Aerospace Sciences and Technologies, Politecnico di Milano, Via La Masa 34.

[‡]Ph.D., Department of Aerospace Sciences and Technologies, Politecnico di Milano, Via La Masa 34.

[§]Adjunct Professor, Department of Aerospace Sciences and Technologies, Politecnico di Milano, Via La Masa 34.

Ω	Rotational Velocity
\mathbf{u}_r	Perturbed Velocity
ω	Vorticity associated to perturbed velocity
ϕ	Potential function
\mathbf{V}_G	Grid Velocity
h	Enthalpy
H	Total Enthalpy ($h + \frac{v^2}{2}$)
γ	Heat capacity ratio
Ψ	Inter Blade Angle
σ	Inter Blade Phase Angle (IBPA)
\mathbf{x}	Grid coordinates
\mathbf{M}	Mass Matrix
\mathbf{C}	Coriolis Matrix
\mathbf{K}_c	Differential Stiffness Matrix due Rotation
\mathbf{F}_c	Inertia Forces related to the motion of the rotating shaft
\mathbf{X}	Modal Base (Eigenvectors)
β	Modal Participation Coefficient
q_∞	Asymptotic dynamic pressure
C_p	Pressure Coefficient
C_T	Thrust Coefficient
C_P	Power Coefficient
η	Propeller Efficiency
\mathbf{H}_{am}	Aerodynamic Transfer Function
\mathbf{Q}_a	Generalized Aerodynamic Forces (GAFs)
g	Damping
SRP	Single Rotating Propeller
CRP	Contra Rotating Propeller
FP	Full Potential
ALE	Arbitrary Lagrangian Eulerian
S^T	Full Potential Solver
AX	Euler based solver

I Introduction

In recent years, there has been a renewed interest in open rotor propulsion systems, because of their fuel-efficient and environmentally friendlier features, despite being more noisier and complex to manufacture. Two common open rotor configurations exist: puller and pusher. Both can have either a SRP or a pair of CRPs.¹ The advantage of using a second propeller stage is that the rotational velocity component (swirl) introduced in the flow field by the first stage is partially realigned to the asymptotic velocity through the second stage, so increasing the effective engine thrust.² As a consequence, CRPs can have a reduced propeller diameter and/or a reduced operating angular velocity compared to SRPs.³ Moreover, reduced propeller diameters grant an easier integration within the aircraft design and higher flight speeds, almost as fast as turbofan powered aircraft. However, noise, fluid-structure and rotor-to-rotor interactions remain key issues to be faced to accomplish the design of open rotors.

The earlier research activities on both SRPs and CRPs⁴ showed that forced excitations occur over the entire flight envelope because of unsteady, unsymmetrical airflows produced by gusts, up-wash from the wing, and airframe-induced flow field distortions. Flight tests pointed out that forced excitation peak occurs in climb and high-speed cruise conditions⁵. Stall flutter occurs primarily at low speed (high blades pitch) and results from blade separated flows, while classical flutter happens at higher speeds, roughly beyond free stream Mach number of 0.6⁶. In recent years, the open rotor research activities have been mainly devoted to noise emissions; as an example, ref.⁷ assesses and optimizes the aeroacoustic characteristics of a common CRP at various flight conditions.

Focusing on the use of FP method in rotordynamics, the two main works on the aeroelastic stability of propfans are Ref.⁸ and Ref.⁹. The authors developed a FP solver for aerodynamic analysis used throughout the research activities in NASA Lewis Research Center⁴. The FP formulation is solved in conservation form by a fully implicit algorithm using an approximately factored sub-iteration at each time step. The simulations are performed onto structured grids and periodic boundary conditions have been implemented across the blade passage to reduce the computational domain. However, only the self-shed wake is considered in the computational domain and only SRP configurations are investigated. Moreover, the FP solver was also expanded to perform calculations in both frequency and time domain and to treat multiple blade passages with independent blade motions.

The purpose of this work is two-fold. On one hand, even if Euler and Navier-Stokes solver are becoming more and more viable tools, it tries to assess the capability of a FP formulation in predicting the aerodynamic behavior of blades. It is shown that an FP solver provides solutions close to those obtained with an Euler flow based solver even in presence of shocks. On the other hand, it picks up the main components to perform flutter analysis within the aeroelastic design of both SRPs and CRPs. In other words, the problem of flutter

in rotordynamics is not deeply tackled, but the instruments needed are validated with the target of studying the CRPs. The FP solver is based on an independent approximation of the density and velocity potential fields. The solution relies on an unstructured, node-based, finite volume approximation with linear shape functions and nonreflecting boundary conditions. Moreover, periodic boundary conditions are implemented to reduce the computational domain and an implicit scheme is exploited for the time integration. Unlike Ref.⁸ and Ref.,⁹ periodic boundary conditions are also applied to the wake discretization and the blade geometry is fully described within the computational domain. Furthermore, the CRP configuration is analyzed with an *ad hoc* technique which allows to study the aeroelastic stability of such system.

Section II describes the employed FP formulation for rotating bodies and the *ad hoc* technique implemented to solve CRP configurations. Section III recalls the theoretical background for solving flexible structures undergoing centrifugal and Coriolis loads. Section IV lists the main elements to perform flutter analysis and also reports the assumptions of this work. Section V compares the results of various analyses for three different blade shapes with literature.

II Aerodynamic Sub-System

This section provides a theoretical background for the aerodynamic modeling suitable for solving the flow field around rotating bodies. Particular attention is provided to the Bernoulli theorem for rotating frames (Section A). Then, the technique developed to model the case of CRP is presented (Section D). Ref.¹⁰ and ref.¹¹ should be consulted for a more detailed presentation of the two-field FP formulation, the numerical scheme described in the mentioned reference is unchanged.

A Bernoulli Theorem for Rotating Frame

It can be demonstrated that the Bernoulli theorem cannot be formulated in a moving system which rotates steadily with angular velocity $\boldsymbol{\Omega}$. The assumption for using a non-inertial frame is that the grid|body is at rest, while the absolute fluid velocity, \mathbf{u} , is the sum of a perturbed and rotational velocity, $\mathbf{u}_r + \boldsymbol{\Omega} \times \mathbf{R}$. Since the rotational velocity $\boldsymbol{\Omega} \times \mathbf{R}$ does not contribute to the mass balance, the continuity equation remains invariant and can be written in the relative system: $\frac{\partial \rho}{\partial t} + \nabla \cdot (\rho \mathbf{u}_r) = 0$. In the case of the momentum conservation law¹², the contribution of the centrifugal force and the Coriolis force must be added to the right hand-side as

$$\rho \frac{\partial \mathbf{u}_r}{\partial t} + \nabla \cdot (\rho \mathbf{u}_r \otimes \mathbf{u}_r) + \nabla p = -2\rho(\boldsymbol{\Omega} \times \mathbf{u}_r) - \rho \boldsymbol{\Omega} \times (\boldsymbol{\Omega} \times \mathbf{R}). \quad (1)$$

Using the vector identity, $\nabla \times (\vec{F} \times \vec{G}) = \vec{F}(\nabla \cdot \vec{G}) - \vec{G}(\nabla \cdot \vec{F}) - (\vec{F} \cdot \nabla)\vec{G} + (\vec{G} \cdot \nabla)\vec{F}$, and defining the local vorticity, $\boldsymbol{\omega} = \nabla \times \mathbf{u}_r$, one obtains

$$\frac{\partial \mathbf{u}_r}{\partial t} + \frac{1}{2} \nabla(\mathbf{u}_r \cdot \mathbf{u}_r) - \frac{1}{2} \nabla(\|\boldsymbol{\Omega} \times \mathbf{R}\|^2) + \frac{\nabla p}{\rho} = \mathbf{u}_r \times (\boldsymbol{\omega} + 2\boldsymbol{\Omega}), \quad (2)$$

where the centrifugal force per unit mass can be written in terms of a centrifugal potential, $\boldsymbol{\Omega} \times (\boldsymbol{\Omega} \times \mathbf{R}) = -\frac{1}{2} \nabla(\|\boldsymbol{\Omega} \times \mathbf{R}\|^2)$. Even under the assumption of an irrotational flow field, $\mathbf{u}_r = \nabla \phi$, and omentropic flow regime, $\nabla s = 0$, the right hand side of Eq. 2 is not null as in the classical inertial formulation:

$$\nabla \left[\frac{\partial \phi}{\partial t} + h + \frac{1}{2} \|\nabla \phi\|^2 - \frac{1}{2} (\|\boldsymbol{\Omega} \times \mathbf{R}\|^2) \right] = \nabla \phi \times (2\boldsymbol{\Omega}). \quad (3)$$

The relative motion is therefore never irrotational but have at least a vorticity component equal to twice the angular velocity $\boldsymbol{\Omega}$. This shows that the relative flow undergoes a solid body rotation equal to $2\boldsymbol{\Omega}$ in the opposite direction to the rotation of the reference frame. In other words, the absolute velocity $\mathbf{u} = \mathbf{u}_r + \boldsymbol{\Omega} \times \mathbf{R}$ cannot be expressed as gradient of a potential quantity because the term $\boldsymbol{\Omega} \times \mathbf{R}$ is rotational ($\nabla \times (\boldsymbol{\Omega} \times \mathbf{R}) = \boldsymbol{\Omega}(\nabla \cdot \mathbf{R}) - \mathbf{R}(\nabla \cdot \boldsymbol{\Omega}) - (\boldsymbol{\Omega} \cdot \nabla)\mathbf{R} + (\mathbf{R} \cdot \nabla)\boldsymbol{\Omega} = 2\boldsymbol{\Omega} \neq 0$). Hence, the Bernoulli theorem cannot be expressed in a non-inertial reference frame.

Eventually, the Bernoulli theorem can only be written in an inertial reference frame because the flow can be irrotational under the special assumptions of isentropic, $\nabla s = 0$, and isoenergetic, $\nabla H = 0$, conditions, without non conservative external forces (which cannot be expressed by a potential function). The Arbitrary Lagrangian Eulerian (ALE) formulation can be used to deal with a rotational motion with constant angular velocity.¹³ Hence, the fluid is at rest and the grid moves with a arbitrary velocity, \mathbf{V}_G . It can be observed that the grid velocity can represent a rototranslating motion, $\mathbf{V}_G = \mathbf{V}_\infty + \boldsymbol{\Omega} \times \mathbf{R}$, so that Bernoulli theorem is the usual

$$\frac{\partial \phi}{\partial t} + \frac{1}{2} \|\nabla \phi\|^2 + \frac{c_\infty^2}{\gamma - 1} \left(\left(\frac{\rho}{\rho_\infty} \right)^{\gamma - 1} - 1 \right) = 0, \quad (4)$$

where ϕ is the perturbed potential, $\nabla \phi = \mathbf{u}_r$. It must be remarked that the potential function ϕ is attached to the moving grid as well as the density function ρ . As a consequence, the perturbed velocity is calculated at each point of the mesh moving with the arbitrary velocity \mathbf{V}_G . Now, the total convected time derivative is introduced as: $\frac{d*}{dt} = \frac{\partial*}{\partial t} + \mathbf{V}_G \cdot \nabla *$, where the transport term is related only to the moving grid, because there are no relative motions between the velocity potential ϕ and the computational mesh. As long as the aerodynamic grid is not deformed during simulation, there is no need to recompute faces speeds, grid normals, volumes or grid coordinates at each time step because the fluid density ρ and the potential ϕ are attached to the grid. The complete formulation of the FP solver used in this work can be founded in ref

^{10,11}.

B Periodic Boundaries

The computational domain for an isolated open rotor can be reduced to a hollow cylinder, where the inner surface represents the hub, while far field boundary conditions must be applied on the external surface. The outer radius is chosen to reduce reflections typical of bounded domains. In case of an asymptotic velocity, \mathbf{V}_∞ , aligned with the angular velocity vector, $\boldsymbol{\Omega}$, the base annulus can be divided into N_b sections, with N_b being the number of blades, so reducing the computational effort. Figure 1 shows the periodic domain division for a generic propeller. The angular velocity allows to define the "outflow" and "inflow" faces of the reduced domain. Periodic boundary conditions are imposed onto these surfaces ($\rho(\mathbf{x}|_{S_{\text{outflow}}}, t) = \rho(\mathbf{x}|_{S_{\text{inflow}}}, t)$ and $\phi(\mathbf{x}|_{S_{\text{outflow}}}, t) = \phi(\mathbf{x}|_{S_{\text{inflow}}}, t)$).

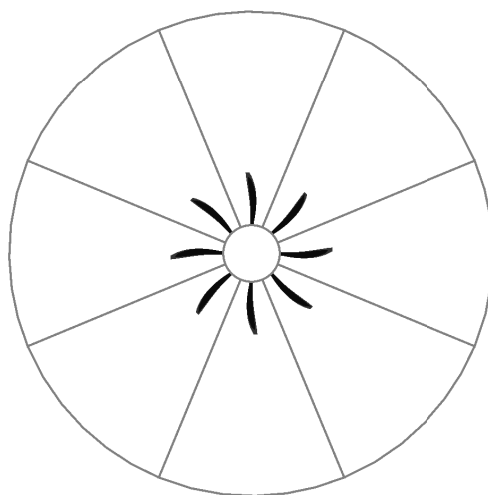


Figure 1: Periodic domain division for a generic 8-bladed rotor.

C Wake Influence and Domain size

A wake discretization must be included in the computational grid. The helicoidal wake is prescribed according to the asymptotic velocity, \mathbf{V}_∞ , and the angular velocity, $\boldsymbol{\Omega}$. Figure 2 shows a typical wake discretization for a periodic domain, where different wake portions are shed by other rotating blades. Figure 3 shows the results of a convergence study to assess the influence of the number of wake portions included in the mesh in terms of rotor thrust. It can be observed that a computational domain containing the wakes shed by a complete rotor revolution provides satisfactory results. Such a property does not change with the propeller pitch angle, β , and with the asymptotic velocity, \mathbf{V}_∞ .

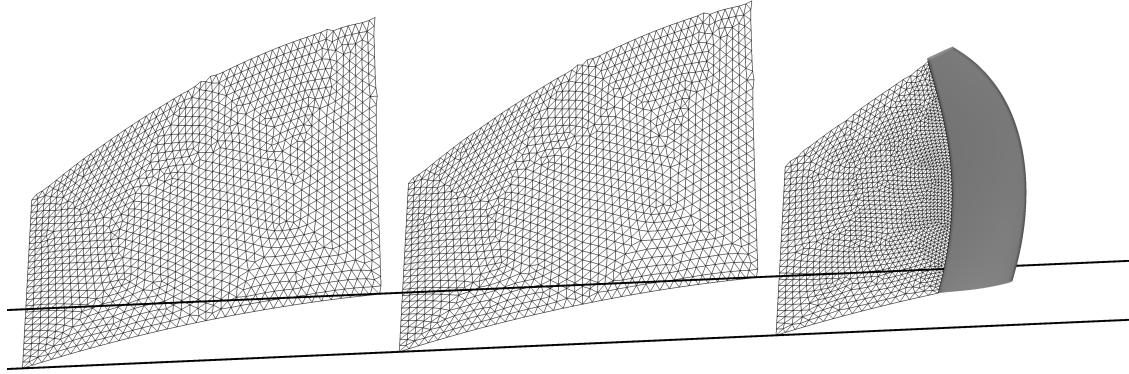


Figure 2: Periodic domain and wake representation for a 3D case.

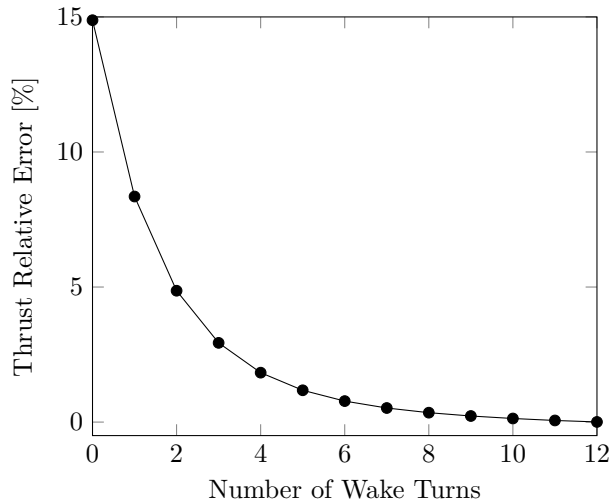


Figure 3: Influence of wake discretization on load for a common 8-bladed rotor.

D Boundary Condition for Contra Rotating Propellers

A common strategy so far adopted to simulate the flow field around different bodies with relative motion is the Chimera method.¹⁴ An alternative strategy consists in simulating the flow field with non-inertial Multiple Reference of Frame (MRF) combined with ALE scheme for the translational motion.¹⁵ Given the rotor angular velocity of a particular domain region, the centrifugal and Coriolis forces can be directly added to the right hand side of the Navier-Stokes or Euler equations.¹² Moreover, Mixing Planes (MPs) are required at the interfaces between regions with different angular velocities. However, the MPs approach cannot be exploited in a FP context because the discontinuity of the potential function (*i.e.* the wake vorticity) cannot be rigorously transferred through the interfaces between regions. Moreover, in a CRP framework, the aft

propeller, as well as its wake, runs into the wake generated by the fore one, so making unsuitable the use of a FP formulation.

As a consequence, an *ad hoc* technique, based on *ghost bodies* and transpiring boundary conditions, is developed. Such a technique avoids the regions interfacing and prevents the difficulties related to the wake-wake or body-wake intersections. The time-marching simulation is replicated in the same number as the

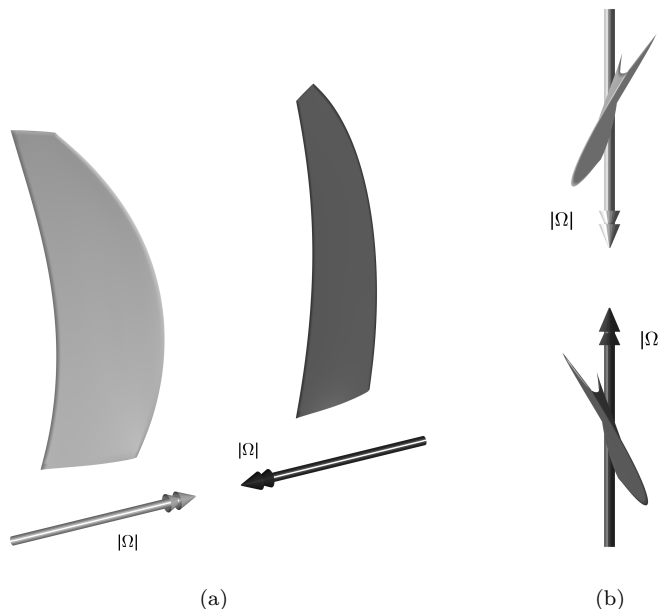


Figure 4: Relative motion between the two rotor blades. In the first simulation, the meshed blade is the black one, while the ghost (gray) is located downstream.

propeller stages. In particular, two simulations linked by proper transpiration boundary conditions are processed simultaneously. When simulating the front rotor the location of the downstream stage in the primary grid is represented by the rear ghost, Figure 4. The velocity potential field, $\phi(\mathbf{x}, t)$, and density field, $\rho(\mathbf{x}, t)$, are evaluated onto the rear ghost contour. Such fields alter the body boundary conditions onto the rear stage of the other simulation with a technique very similar to the transpiration boundary condition. Vice-versa, when simulating the rear rotor, the location of the upstream stage in the primary grid is represented by the front ghost. The velocity potential field, $\phi(\mathbf{x}, t)$, and density field, $\rho(\mathbf{x}, t)$, are evaluated onto the front ghost contour. Such fields alter the body boundary conditions onto the front stage of the other simulation. Since the two propellers counter rotate as shown in Figure 4, the real body (black) is fixed while the ghost (gray) rotates with a doubled angular velocity along the opposite direction in the two parallel simulations. Thus, in the case of two propellers with the same number of blades, N_b , it is possible to define the angle

$$\Psi = \text{Remainder} \left(2\Omega t \div \frac{2\pi}{N_b} \right), \quad (5)$$

as depicted in Figure 5. The angle Ψ is constrained between 0 rad and $\frac{2\pi}{N_b}$ rad. The domain of both simulations is replicated as shown in Figure 5, so allowing to evaluate the mass density and velocity potential fields at the ghost location even when the ghost goes through a periodic boundary.

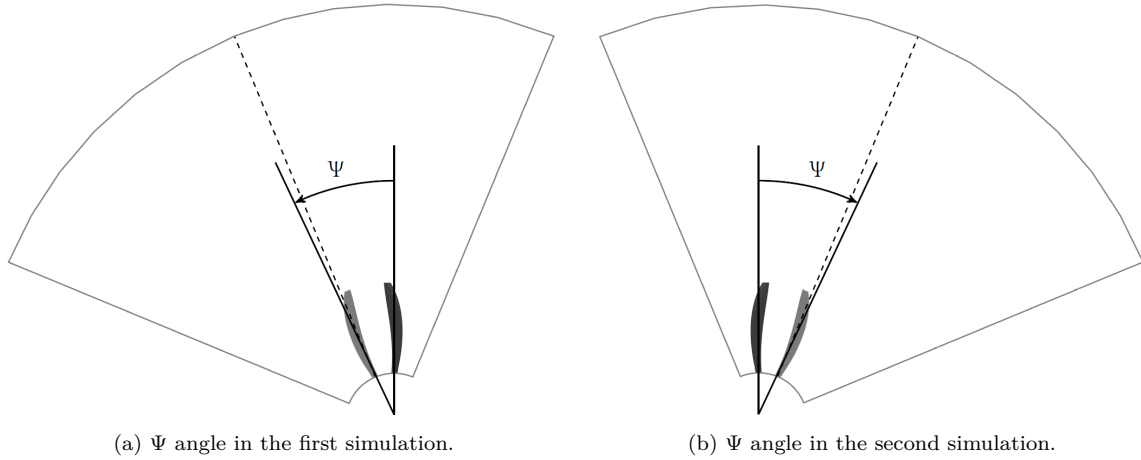


Figure 5: Visualization of the Ψ angle in both cases.

The superposition of the solutions of the two simulations approximates the total flow field around the two lifting bodies. The effectiveness of this technique relies upon the superposition principle. Although the compressible aerodynamics is nonlinear, the (ab)use of the superposition principle gives good results for a weak coupling between the two propellers so allowing to linearize the problem. This technique can give a fair representation of the linearized instationary aerodynamics due to the blade motions, so well matching within the framework of stability analysis. In such a view, there is no need to fully represent the complex CRP aerodynamic behavior which demands an high computational cost.

The perturbation introduced by the *ghost* has to be taken into account in the boundary conditions of the real body (*i.e.* the black one in Figure 4 and Figure 5). As a consequence, the density flux at the solid boundaries becomes:

$$F_{body} = - \int_{\Gamma_b} (\rho_0 + \Delta\rho) \nabla(\Delta\phi) \cdot \bar{n} d\Gamma_b, \quad (6)$$

where $\rho_0(\mathbf{x}, \bar{t}_k)$ is the density field evaluated onto the real body at iteration k , while $\Delta\rho(\mathbf{x}, \bar{t}_{k-1})$ and $\Delta\phi(\mathbf{x}, \bar{t}_{k-1})$ are the perturbations of the density field and potential field evaluated onto the *ghost* body at the previous iteration. At each time step, the solution of both stages converges after few iterations.

The procedure above exposed is validated with a 2D test case. The flow field around two misaligned NACA 0012 airfoils with chord $c = 1$ m is considered. The airfoils are 1 m away from each other in both directions and the asymptotic velocity direction sets an angle of attack of 2 degrees. The reference solution is obtained with the domain represented in Figure 6 while the *ghost technique* is applied to a domain containing

only one airfoil.

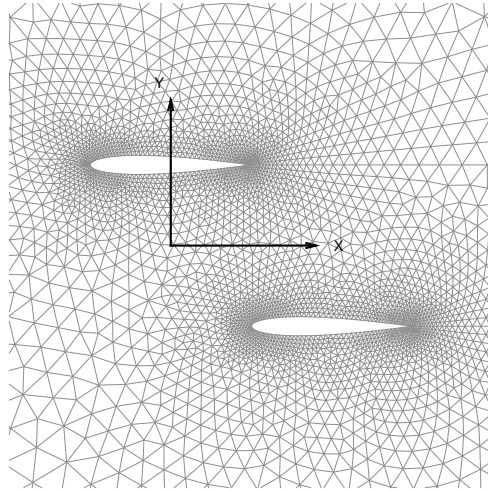


Figure 6: Detail of the computational grid.

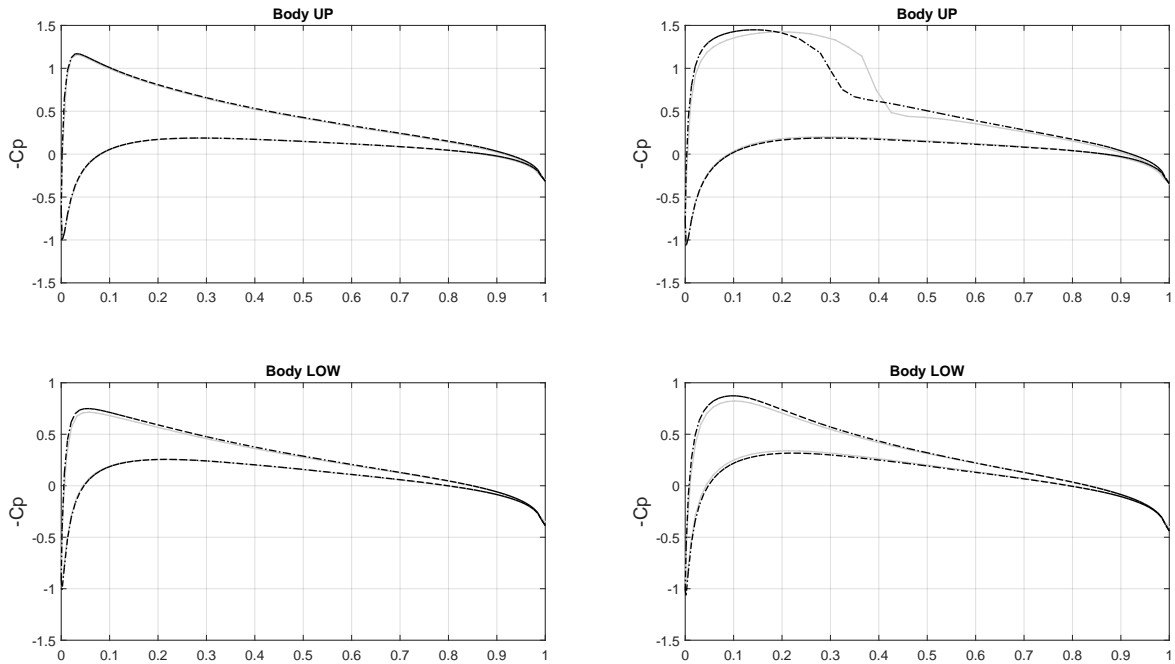
The pressure coefficient distributions above the airfoils for both the case of $M_\infty = 0.5$ and $M_\infty = 0.7$ are reported in Figure 7. The comparisons of the density fields, $\rho(\mathbf{x}, t)$, between the reference simulations and the ones obtained with the proposed *ghost technique* are showed in Figure 8 and Figure 9. It can be seen that the obtained solutions are very similar in the subsonic flight condition, *i.e.* $M_\infty = 0.5$. In addition, it can be inferred that the technique works like a "superposition of effects", so it gives a very good approximation if the coupling between the two separated flow field solutions is not very strong.

III Structural Sub-System

The periodicity of the domain can be exploited also to simplify the structural analysis. Usually, the hub is not considered when modelling the rotor because it is significantly stiffer than the blades. So, the blades can be approximated as structurally independent bodies, interacting with each other through the aerodynamics.

A Reference Frames and Kinematic Relations

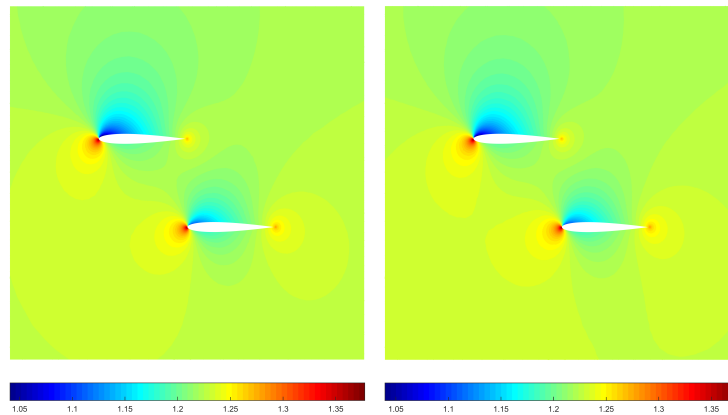
The centrifugal and the Coriolis loads act on a steadily rotating structure, and the dynamic response of the blades is strongly affected by these actions. The use of a rotating reference system is the simplest approach to formulate the dynamic equations. As explained in ref.,¹⁶ the coordinates of a generic point of a rotating structure is defined using three different coordinates systems: an inertial reference system (to which relate accelerations and inertial forces); a reference system associated to the mean motion of the undeformed disk,



(a) $M_\infty=0.5$

(b) $M_\infty=0.7$

Figure 7: Pressure Coefficient distributions over the airfoils. (●) for *reference* solution, (- - ●) for *ghost* solution.



(a) *Reference.*

(b) *Ghost.*

Figure 8: Mass Density for $M_\infty = 0.5$.

which is defined by a new origin \mathbf{x}_0 and by a rotation matrix $[\boldsymbol{\alpha}]$; a reference system related to the perturbed motion of the disk, which is defined by a perturbation $\Delta\mathbf{x}_0$ and by a perturbation of the rotation matrix

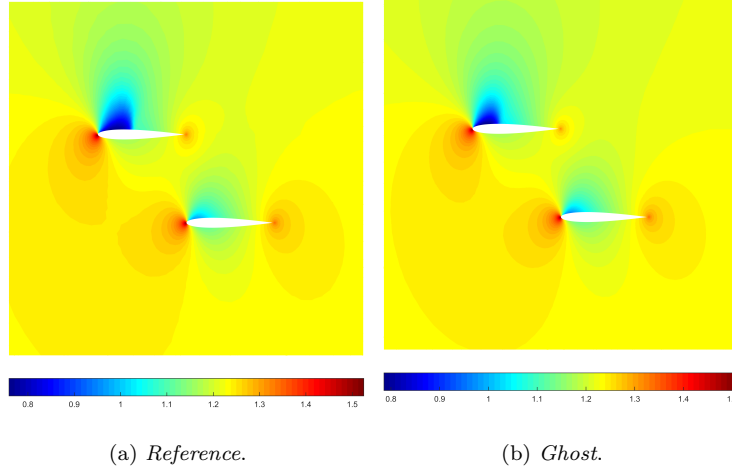


Figure 9: Mass Density for $M_\infty = 0.7$.

$[\Delta\mathbf{\Gamma}]$. Using this description, the generic coordinates of a body point are:

$$\mathbf{x} = \mathbf{x}_0 + [\alpha] \Delta\mathbf{x}_0 + [\alpha] [\Delta\mathbf{\Gamma}] (\mathbf{r} + \mathbf{u} + \Delta\mathbf{u}), \quad (7)$$

where the position is given by the undeformed location \mathbf{r} plus a displacement, which is separated into a trimmed (steady condition) contribution \mathbf{u} and a dynamic perturbation contribution $\Delta\mathbf{u}$.

B Virtual Work Principle of Inertial Forces

The virtual work of the inertial forces, can be expressed as

$$\delta W^i = \int_{\mathcal{V}} \delta \mathbf{x}^T \rho \ddot{\mathbf{x}} d\mathcal{V} = \delta \mathbf{w}^T (\mathbf{M} \dot{\mathbf{w}} + \mathbf{C}_c \dot{\mathbf{w}} + \mathbf{K}_c \mathbf{w} + \mathbf{F}_c), \quad (8)$$

where \mathbf{F}_c represents the generalized inertial forces related to the mean motion of the structure. These forces are in equilibrium with the elastic ones and with external loads related to the mean motion. In this way, the elastic trim of a rotating structure is computed. The matrix \mathbf{K}_c introduces the stiffness effect of the centrifugal load. It can be demonstrated that there is a stiffening effect due to the tensile stresses caused by rotation and a softening one due to the non inertial frame in which the equations are written. In common application, they combine to give a stiffness net effect but in some cases a centrifugal softening effect is found (but limited in magnitude) and occurs at spin speed so high that cannot be reached without jeopardizing the mechanical integrity of the rotor.⁷ The matrix \mathbf{C}_c represents the effect of Coriolis forces. Indeed, it is an apparent damping because Coriolis forces do not work for a virtual displacement. The contribution to damping of the Coriolis forces is always negligible when the blades are clamped to a rotor hub rotating along a fixed direction. Ref.¹⁷ presents a detailed dissertation about the effects of centrifugal and Coriolis forces on the mode shapes and frequencies of a rotating system.

C Virtual Work Principle of Elastic Forces

The virtual work of the generalized internal forces generates a stiffness matrix. For a general analysis, such a matrix can be partitioned as,

$$\mathbf{K} = \begin{bmatrix} \mathbf{K}_{x_0x_0} & \mathbf{K}_{x_0\psi} & \mathbf{K}_{x_0q} \\ \mathbf{K}_{\psi x_0} & \mathbf{K}_{\psi\psi} & \mathbf{K}_{\psi q} \\ \mathbf{K}_{qx_0} & \mathbf{K}_{q\psi} & \mathbf{K}_{qq} \end{bmatrix} \quad (9)$$

where there are the coupling terms between rigid motion and deformable displacements. As already mentioned, our concern is related to \mathbf{K}_{qq} , because the other terms are mainly related to the support compliances. In this work, the support is supposed to be perfectly rigid without any relative motion respect to the rotating frame, so only the term \mathbf{K}_{qq} is needed.

Expressing displacements with proper shape functions, one obtain the matrix form of internal virtual work¹⁸

$$\delta W_d = \delta W_d^0 + \delta \mathbf{q}^T \bar{\mathbf{K}} \mathbf{q}. \quad (10)$$

where: $\delta W_d^0 = \int_V \boldsymbol{\varepsilon}^{0T} \mathbf{S}^0 dV$, $\bar{\mathbf{K}} = \mathbf{K}_e + \mathbf{K}_G$. There are two contributions to the matrix \mathbf{K}_e : the *linear stiffness* \mathbf{K} , which is the common stiffness in small deformation and small displacement problems, and the so-called *geometric stiffness* \mathbf{K}_L , which is related to the deformed shape in the reference condition. In addition, the *prestress stiffness* \mathbf{K}_G is related to the stress field in the reference configuration.

D Numerical Procedures

The main solver work-flow consists in: 1) Assembly and factorization of various matrices; 2) Trim with centrifugal loads; 3) Compute the *prestrain* and *stress stiffness* matrix (with the displacement field just calculated); 4) Solve the eigenproblem (frequencies and modes); 5) Build the reduced system. The first four points will be carried out in commercial softwares, NASTRAN[®] and Ansys[®]. The approach of the two commercial softwares is documented in ref.¹⁹ and ref.²⁰ respectively. Examples of a proper use of various parameters are reported in chapter V.

E Building the reduced system

The eigenproblem without rigid motions and without the inertial damping matrix \mathbf{C}_c is

$$\omega^2 \mathbf{M} \Delta \mathbf{q} = (\mathbf{K}_e + \mathbf{K}_G + \mathbf{K}_c) \Delta \mathbf{q}. \quad (11)$$

As already mentioned, the support is here supposed to be perfectly rigid without any relative motion with respect to the rotating frame, so the contribution of the matrix \mathbf{C}_c can be neglected. In this way, the natural frequencies remain imaginary and eigenvectors become real, since no other form of dissipation are

introduced. In the case of flexible support, the gyroscopic effects introduced by \mathbf{C}_c are significant and directly proportional to the angular spin rate. The complete linearized reduced system is

$$\mathcal{M}\ddot{\beta} + \mathcal{C}\dot{\beta} + \mathcal{K}\beta = 0, \quad (12)$$

where: $\mathcal{M} = \mathbf{X}^T \mathbf{M} \mathbf{X}$, $\mathcal{C} = \mathbf{X}^T \mathbf{C}_c \mathbf{X}$, $\mathcal{K} = \mathbf{X}^T \mathbf{K} \mathbf{X}$ and \mathbf{X} is the selected modal base. The size of the reduced model depends on the level of approximation required. In aeroelastic analysis, few modes can generally describe the structural subsystem fairly well. This model condensation is very useful to efficiently conduct flutter calculations.

IV Flutter Analysis

Assuming small perturbations, the motion of one blade generates unsteady loads on the neighboring blades and these in turn affect the reference one with a linear superposition of forces. It can be inferred that

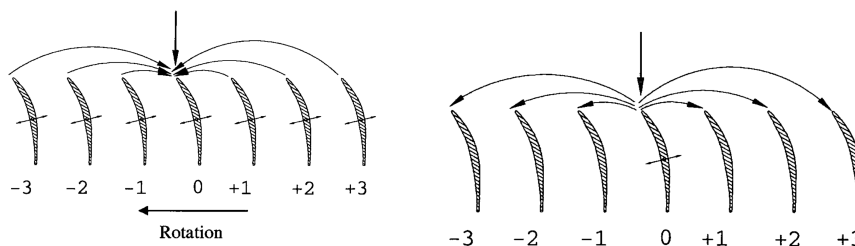


Figure 10: Physical explanation of influence coefficients, ref.²¹

the perturbations affecting the reference blade (*i.e.* "0" in Figure 10) do not act simultaneously but with a precisely time delay. So, in the field of aeroelastic analysis, more complex periodic boundary conditions must be introduced to correctly represent the lag of the perturbations coming from the motion of other blades if only one blade is modelled. The concept of the *Inter Blade Phase Angle* (IBPA²²) becomes an important parameter, along with the more traditional reduced frequency $k = \frac{\omega L_a}{V_\infty}$. The IBPA can take only N_b integer values, $\text{IBPA} = n\sigma$, with $n = 0, \dots, N_b - 1$ and $\sigma = \frac{2\pi}{N_b}$. The simplest way to represent the complex aero-structural behavior is to simulate the whole rotor. As in turbomachines applications,^{22,23} IBPA can be treated by extending the periodic domain to $n+1$ blades. Only one blade (*i.e.* $\text{IBPA} = 0^\circ$) is here considered for flutter analysis due to the limited computational resources of a common personal computer. Although all the IBPA should be investigated, the partial results obtained can give a first glimpse on the stability.

A Aeroelastic Problem Build-Up

The aerodynamics loads are added to the right hand side of the Eq. 12,

$$\mathcal{M}\ddot{\boldsymbol{\beta}}(t) + \mathcal{C}\dot{\boldsymbol{\beta}}(t) + \mathcal{K}\boldsymbol{\beta}(t) = \boldsymbol{Q}_a(t), \quad (13)$$

where \mathcal{M} , \mathcal{C} and \mathcal{K} are the generalized mass, damping and stiffness matrices of Section III. The array of the GAFs, $\boldsymbol{Q}_a(t)$, is assembled by projecting the aerodynamic pressure field $C_P(\boldsymbol{x}, t)$ acting on the body surface S onto the structural modal base \boldsymbol{X} ,

$$\boldsymbol{Q}_a(t) = q_\infty \int_S C_P(\boldsymbol{x}, t) \boldsymbol{N}(\boldsymbol{x})^T \vec{n} dS = q_\infty \boldsymbol{H}_{am} \boldsymbol{\beta}. \quad (14)$$

The aerodynamic transfer functions matrix, namely $\boldsymbol{H}_{am}(\sigma_n, k, M_\infty)$, can be evaluated directly in the Laplace domain. However, such an approach can involve undue computational costs using nonlinear aerodynamic models to determine a basic reference condition needed for the linearization because a precise evaluation of the aerodynamic Jacobian matrix must be performed at each desired steady state. So, the matrix $\boldsymbol{H}_{am}(0^\circ, k, M_\infty)$ is here obtained through time marching simulations. At first, the steady solution for the aeroelastic system must be reached. Then, the vector of the GAFs, $\boldsymbol{Q}_a(t)$, due to a prescribed law of motion of the i -th generalized displacement $\beta_i(t)$ can be computed. The i -th column of the aerodynamic transfer functions matrix $\boldsymbol{H}_{am}(0^\circ, k, M_\infty)|_i$ is the ratio between the Fourier transform of the output and input signal of the aerodynamic system. Performing such an operation for each structural degree of freedom (*i.e.* the modal basis $\boldsymbol{\beta}$) the whole aerodynamic transfer functions matrix $\boldsymbol{H}_{am}(0^\circ, k, M_\infty)$ is obtained. The law of motion for the i -th generalized displacement $\beta_i(t)$ must excite the desired reduced frequency range $[0, k_{max}]$. Moreover, the amplitude of the displacement must be large enough to overcome the numerical noise but not too large to preserve the small perturbation hypothesis. The better choice is likely a blended step input which allows just one test for each input to characterize completely the system in the whole frequency range of interest.

B Flutter Calculation

Moving to the Laplace domain and recalling the expression of the GAFs, Eq. 14, the structural problem, Eq. 13, falls in the framework of classical aeroelasticity as an algebraic homogeneous system,

$$[s^2\mathcal{M} + s\mathcal{C} + \mathcal{K} - q_\infty\boldsymbol{H}_{am}(p, M_\infty)] \boldsymbol{\beta}(s) = [A(s, V_\infty)]\boldsymbol{\beta}(s) = 0. \quad (15)$$

Such a system admits non-trivial solutions if the matrix $[A(s, V_\infty)]$ is singular and is closed in the complex unknown s for a given velocity V_∞ . Starting from $V_\infty = 0$, the roots loci can be found for the whole flight envelope. The so-called $V_\infty - \omega$ and $V_\infty - g$ diagrams, where $g = 2\sigma/\sqrt{\sigma^2 + \omega^2}$ (σ and ω are the real and imaginary parts of a complex number respectively), suitably represent the stability properties of the system. The first intersection in the $V_\infty - g$ diagram with the V_∞ axis identifies the flutter velocity, *i.e.* the zero damping condition. The complex eigenvalue problem to be solved depends on the way in which the aerodynamic loads are included in the equations of motion or whether certain damping terms are considered.

The two methods for flutter analysis used in this work are summarized in next sections. First, the K-E method is used for sake of comparison with the flutter analysis already provided in the literature. In this way, the validation of the procedures before described can be proved. Then, a variation of the well-known $p - k$ method²⁴ is exploited. The develop of a modified $p - k$ method is mandatory because it can involve some difficulties in tracking intersecting eigenvalues. The approach used here prevents such a drawback because each mode is tracked separately from the others.

K-E(FICIENT) METHOD This method is a simplification of *K-method* in which all viscous sources of the structure or of the control system are neglected. The equations of the *K-method* are

$$\left[-\omega^2 \mathbf{M} + j\omega \mathbf{C} + (1 + jg)\mathbf{K} - \left(\frac{1}{2}\rho V^2\right) \mathbf{H}_{am}(k, M_\infty) \right] \boldsymbol{\beta}(\omega) = \mathbf{0}, \quad (16)$$

where g is an artificial structural damping. Note that k , V_∞ and ω are not independent and usually the term \mathbf{C} is deleted (complex structural damping may still be included in \mathbf{K}). The values of g , V_∞ , and f are determined for various values of M_∞ , k , and ρ . The flutter occurs where g goes through zero to positive values.

Ref.²⁵ uses this method to predict flutter boundaries and so it is a useful test case for validating the formulation proposed to carry out the aerodynamic transfer function \mathbf{H}_{am} . The results obtained are reported in next section.

FLUTTER EIGENSOLUTION AS A NONLINEAR PROBLEM The aeroelastic problem, Eq. 15, can be seen as a linear homogeneous system in $\mathbf{q}(s)$ and nonlinear in s .^{26,27} So, a normalization rule for the generalized coordinates vector $\mathbf{q}(s)$ can be added to close the problem,

$$\begin{cases} \mathbf{A}(s, V_\infty)\boldsymbol{\beta} = 0 \\ \frac{1}{2}\boldsymbol{\beta}^T \mathbf{W}\boldsymbol{\beta} = 1 \end{cases}, \quad (17)$$

where $\mathbf{W} = \text{diag}(W_i)$ for $i = 1, \dots, n$ (in which n is the number of modes used to reduce the aeroelastic system) are arbitrary weights. The obtained nonlinear system can be solved through the *Newton-Raphson* method. Linearizing around a reference solution β_0 and s_0 we obtain,

$$\begin{bmatrix} \mathbf{A}(s_0, V_\infty) & \left. \frac{\partial \mathbf{A}(s, V_\infty)}{\partial s} \right|_{s_0} \beta_0 \\ \beta_0^T \mathbf{W} & 0 \end{bmatrix} \begin{Bmatrix} \Delta \beta \\ \Delta s \end{Bmatrix} = \begin{Bmatrix} -\mathbf{A}(s_0, V_\infty) \beta_0 \\ 1 - \frac{1}{2} \beta_0^T \mathbf{W} \beta_0 \end{Bmatrix}. \quad (18)$$

Such an approach allows to compute the eigenvalue and the eigenvector all at once. Starting from $V_\infty = 0$ with $\beta = \beta_0$ and $s = s_0$, *i.e.* the structural solution, $V_\infty - \omega$ and $V_\infty - g$ diagrams can be plotted. The procedure must be repeated starting from each structural eigenvalue avoiding any problem with intersecting curves. In this way, the whole eigensolution is tracked with a very simple task and without the drawback of intersecting eigenvalues. Since the aerodynamic transfer functions matrix $\mathbf{H}_{am}(k, M_\infty)$ is known for a set of reduced frequencies only, an interpolation technique is required.

NUMERICAL PROCEDURES A trial transport jet is identified in order to prevent flutter in its flight envelope. In this way, an high fidelity polar is built using the preliminary design methods of ref.²⁸. Once Penaud diagrams are obtained, the trimmed condition (Thrust = Drag) is imposed for a steady rectilinear flight at a discrete number of blades pitch and various altitudes. At the end of the trim calculations, every selected pitch angle is matched with an asymptotic velocities V_∞ . In particular, the blade pitch angle is referred to the plane of rotation of the rotor disk. As an example, Penaud diagram of the test case of Section C at sea level is reported in Figure 11. Then, the aerodynamic transfer function are calculated at every trimmed condition (red squares of Figure 11). Finally, the $V_\infty - g$ and $V_\infty - \omega$ diagrams are obtained by a flutter calculation as a solution of a nonlinear problem.

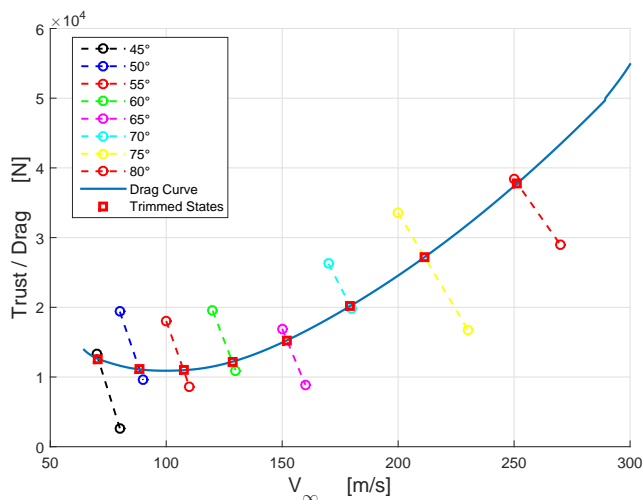


Figure 11: Penaud Diagram at $h = 0$ m.

C Contra-Rotating Propeller

Since the system is periodic due to the combination of the rotational motion of the two rotors, the classical theory for predicting instabilities for Linear-Time-Invariant (LTI) system cannot rigorously be used. For the case of Linear-Time-Periodic (LTP) systems, the somewhat more complex Floquet theory must be used to correctly predict the instability boundaries. Moreover, the cascade effects due to non-zero IBPA must be accounted for, as in the case of the linearized turbomachines flutter analysis.²³ Such effects modify the damping g of the system and they are not always negligible²⁹. Besides, the $\mathbf{H}_{am}(\bar{\sigma}, k, M_\infty)$ matrix at a particular flight condition and IBPA ($\bar{\sigma}$) is a 2×2 block matrix, whose main diagonal contains the aerodynamic influences between the blades of the same rotor while the antidiagonal contains the mutual aerodynamic influences between the blades of the two stages.

However, thanks to the small variation of the aerodynamic loads around the equilibrium condition, a simplification of the Floquet theory can be exploited. Systems that shows small variation around an equilibrium state are also called *small varying systems*. In particular, ref.³⁰ explains which conditions are required for a linear stability of the response of such LTP system. In the field of classical aeroelasticity, the heavier calculation is the correct identification of the GAFs in the frequency domain. In addition, since the signal is periodic, the frequencies spectrum presents many peaks. In the case of two stage with the same number of blades, N_b , the peaks occur at $\omega_i = 2\Omega N_b i$, for $i = 1, 2, \dots$, where Ω is the angular velocity. As an example, Figure 12a shows the frequency magnitude of a front rotor thrust coefficient, C_T . In this example, since $\Omega = 895$ RPM and $N_b = 8$, the fundamental harmonic is $\omega_1 = 2\Omega N_b = 238$ Hz. Basically, the idea is to remove the peaks of the various multiples of the fundamental harmonic from the aerodynamic transfer functions $\mathbf{H}_{am}(0^\circ, k, M_\infty)$, thus obtaining a non-periodic signal in the time domain. In other words, the real and imaginary part of the Fourier coefficients are filtered in some way in order to extract the variation of the GAFs from the time-periodic equilibrium solution (*e.g.* see Figure 12b). The most simple process is to use a low pass filter, *e.g.* Butterworth, with a cut-off frequency lower than the fundamental harmonic, $\omega_1 = 2\Omega N_b$. Finally, particular attention must be given to the blended step input of β_i in the periodic oscillation of GAFs because of the time marching simulation. The transient of such perturbation input must be lesser than one period so simulating nearly a step. In particular, the chosen input transient have to last about an half of a oscillating period, so that the induced perturbations expire within a period at most. In this way, the assumption of a "frozen" stability analysis³⁰ is acceptable because both the change of the aerodynamic boundary conditions and the transient system responses are very quick; so the stability of such LTP responses can be justifiably treated like a common LTI system.

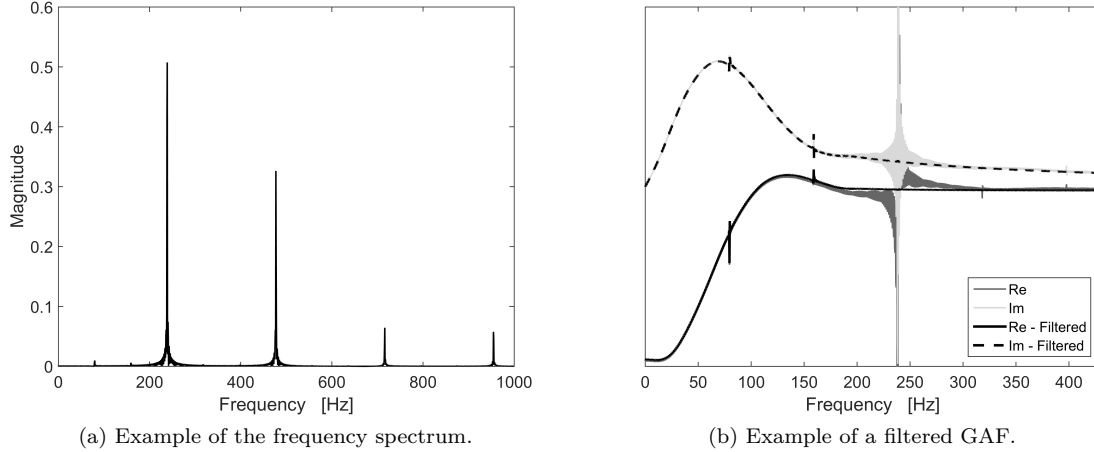


Figure 12: GAF processing methodology.

V Results

This section assesses the effectiveness of the proposed approach for the aeroelastic analysis of open rotor by comparing the results obtained with the FP formulation, S^T (ref.^{10,11}), against reference data available in the literature and with those obtained through the Euler flow solver, *AeroX* (ref.^{31,32}). The aerodynamic analyses performed with both S^T and *AeroX* are carried out with the same grids. The theoretical methods described in Section IV have been validated in ref.³³ by analyzing the flutter boundary of a typical section and of the AGARD 445.6 wing. Now, we tackle the aeroelastic problem of rotating wings in order to analyze the flutter boundaries of both SRP and CRP. It must be remarked that the purpose of this work is far from a deep study of flutter but the methodology is validated through various test cases.

Four different test cases are investigated. Section A is dedicated at assessing the potentialities of the full potential solver S^T with aerodynamic analyses of SRP and CRP. Section B presents a complete aeroelastic analysis in accordance with ref.²⁵ These two test cases represents the validation|verification benchmarks of the proposed aeroelastic analysis technique. In Section C and in Section D the aeroelastic analyses are conducted without reference to any result available from the literature, but only on the base of the awareness gained from the previous benchmarks. In particular, the first section is focused on an SRP, while the following one discusses the stability of a CRP.

A TEST CASE 1

This test case shows the potentialities of the solver S^T for assess the flow field around rotating bodies. The blade geometry is taken from ref.⁷ Figure 13 shows the radial distributions of the thickness normalized by the chord, t/c , the blade mean-line sweep angle, Φ , as well as the twist distribution of the blade, β . The

selection of the blade airfoils is set in accordance to the approach of the SR-7L high-speed propeller reported in ref.⁶ The blade features NACA65-series airfoils near the root to the radial position of $r/R = 0.4$ then transitioning to NACA16-series airfoils from $r/R = 0.55$ outward. The mean-line tip sweep is $\Phi = 35^\circ$. The rotor diameter is $D = 4.2672$ m and the hub-to-tip ratio is $d/D = 0.355$.

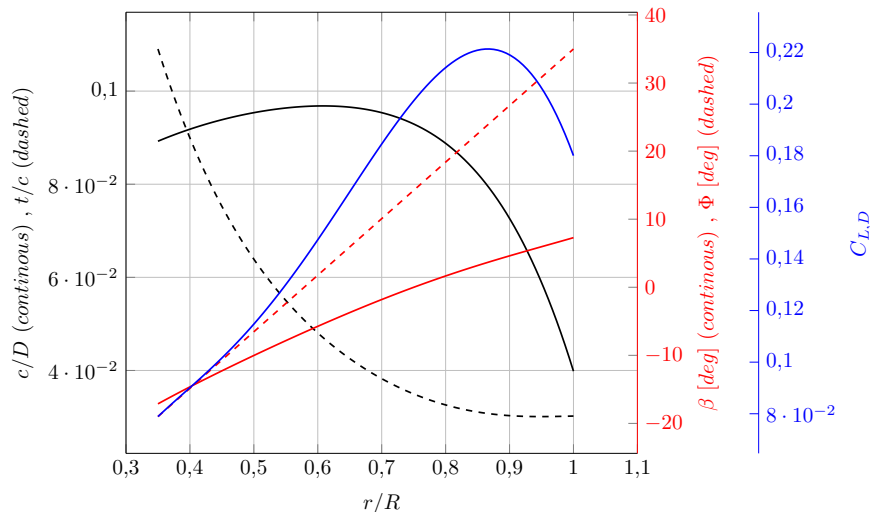


Figure 13: Blade Characteristics taken from ref.⁷

1 Aerodynamic Analyses of a Single Rotating Propeller (SRP)

First, the simple case of an 8-blade SRP is investigated. Ref.⁷ carried out its simulations using the DLR-TAU-code,³⁴ with Spalart-Allmaras turbulence model. Ref.⁷ fully exploits the Chimera functionality,³⁵ so enabling a variation of the blade pitch settings without any re-meshing. The simulations are carried out at the design cruise condition with a propeller rotational speed of $\Omega = 895$ RPM. The pitch angle at 75% of the blade span, $\beta_{75\%}$, varies from 56° to 63° with the flight condition reported in Table 1. This flight

M_∞	h [m]	ρ_∞ [Kg/m ³]	P_∞ [Pa]
0.75	10668	0.4135	26500

Table 1: Flight Conditions.

condition leads to a tip Mach number of $M_{tip} = 1.0068$, so that weak shocks are expected on the blade surface. The geometric angle of attack remains always under 5° at the 75% of the blade span. A small flow separation being nonetheless generated by the weak shock onto the outer surface. For such an application, S^T gives acceptable results. Figure 14 reports comparisons of the thrust coefficient $C_T = \frac{T}{\rho n^2 D^4}$, the torque coefficient $C_l = \frac{\mathcal{C}}{\rho n^2 D^5}$, the power coefficient $C_P = 2\pi C_l$ and propeller efficiency $\eta = \frac{C_T}{C_l} \frac{J}{2\pi}$, where $n = \Omega/2\pi$ is the propeller rotational speed, $J = V_\infty/(nD)$ is the advance ratio, $\mathcal{C} = \rho n^2 D^5 C_l$ is the torque. uRANS results show a good accordance to those obtained with S^T while the Eulerian solver *AeroX*

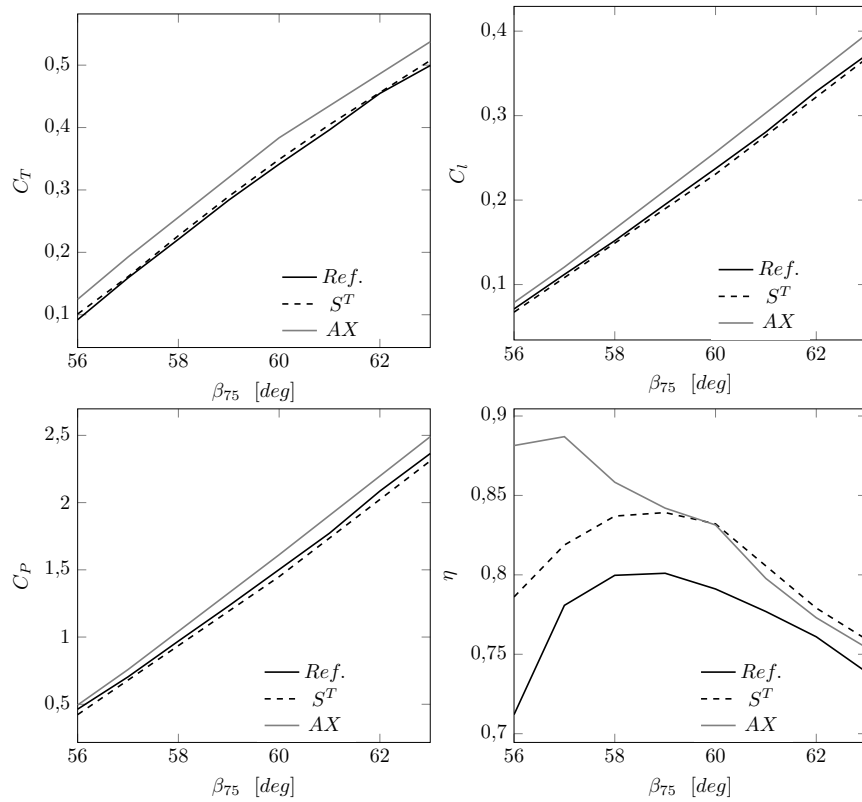


Figure 14: Comparison between the results obtained by CFD analysis of ref.,⁷ S^T and AX.

provides worse somewhat correspondences, in particular for the efficiency η . The differences can be imputed to the effects of the boundary layer that cannot be modelled in an Euler|potential solution and to different numerical schemes adopted. Anyhow, this testcase shows that full potential solvers can be valuable tool for predicting the performances of SRP. Figure 15 shows the Mach and C_p fields respectively onto the upper surface of the blade for the steady state obtained with $\beta_{75\%} = 60^\circ$. As said, the local Mach number reaches transonic values and a weak shock extending from the tip to the root of the blade can be observed.

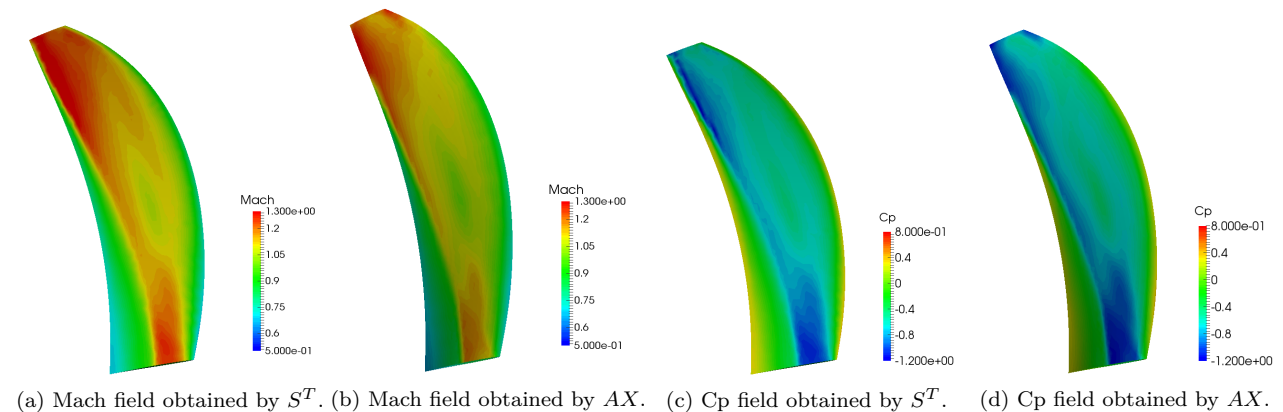


Figure 15: Comparison between Mach and C_p fields.

2 Aerodynamic Analyses of a Contra-Rotating Propeller

In the case of CRPs, the total thrust is equally partitioned between the two propeller. The operating conditions are the same as the SRP case reported in Table 1. The "ghost technique", explained in Section II, is here verified to work reasonably.

Table 2 shows a good accordance for the pitch angles at 75% of blade span. The differences in the set angles are lower than 1° . This error can be imputed to the different approaches used to describe such a periodic system. Moreover, the details modelled in our mesh are significantly less than those of the grid of ref.,⁷ which models the whole engine.

	Ref. ⁷	S^T
Front Rotor $\beta_{75\%}$	61.0 °	60.5 °
After Rotor $\beta_{75\%}$	57.9 °	57.0 °

Table 2: Blade Pitch Angle at 75% of span-wise direction for equally partitioned thrust between the two rotors at an angular velocity of $\Omega = 895$ RPM and at an altitude of 10000 m.

Figure 16 shows the thrust coefficients of the separated rotors. The periodic nature of the loads is related to the body-body and body-wake interactions of the two propellers. Table 3 reports the comparison of the mean values of the C_T , C_P and η at regime. The potential solver underestimates the torque required because the viscous drag forces acting on the blade are not included. This fact involves lower power coefficients, and so greater efficiency with respect to those calculated with a uRANS simulation.

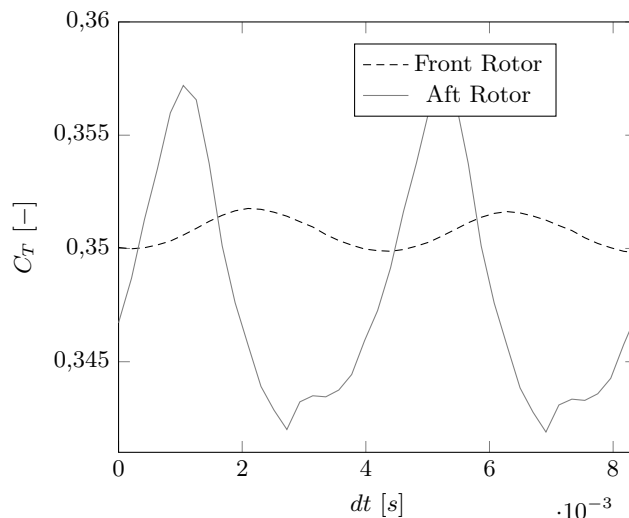


Figure 16: Thrust coefficient C_T of the front and aft rotor.

	Front Rotor			Rear Rotor		
	C_T	C_P	η	C_T	C_P	η
Ref. ⁷	0.3372	1.5956	73.85%	0.3379	1.4838	79.58%
S^T	0.3507	1.4544	83.33%	0.3486	1.2649	95.26%

Table 3: Comparison of the most important parameter of CRP.

B TEST CASE 2

The flutter analyses of the *SR* – 5 propfan, a 10-blade wind tunnel model designed by Hamilton Standard in early '80s during the ATP project, is carried out. This blade has a tip sweep of 60° , the maximum value allowed for a metal blade without excessive stresses, a medium chord of 7.67 cm and a span of about 30 cm. During performance testing in the Lewis transonic wind tunnel, the *SR* – 5 propeller encountered classical bending-torsion flutter above $M_\infty = 0.7$.

1 Structural Modal Analysis

The structural grid is taken from ref.³⁶ The blade is discretized only with shell elements and is fully constrained at its base. Table 4 reports the first 6 normal frequencies for the rotating blade at an angular velocity of 6800 RPM.

#	<i>type</i>	Ref. ³⁷ NASTRAN		Ref. ³⁸
		CQUAD8	CQUAD4	HEXA
1	1st Flap	187.9	170.9	173.7
2	2nd Flap	292.8	287.0	285.4
3	1st Tors	612.6	595.9	598.4
4	1st Tip Flap	666.9	670.7	647.2
5	2nd Tip Flap	822.3	863.2	816.8
6	2nd Tors	1008.5	1013.4	970.0

Table 4: Rotating Normal Frequencies [Hz] of the SR-5 blade.

2 Aerodynamic Analysis

Table 5 reports the four wind tunnel test conditions for the SR-5 propfan taken from.³⁷ In all the cases, the local Mach number at the blade tip always reaches transonic values. Unfortunately, the cases 1 and 4 cannot be simulated for numerical problems related to the combination of high asymptotic Mach number M_∞ and mean angle of attack. In this cases, S^T does not converge at a steady solution because the angle of attack is too high (about 15°) in relation to the asymptotic Mach number $M_\infty = 0.85$. Thus, only the results from cases 2 and 3 are compared with those available from the literature and from *AeroX*. The maximum local

Case No.	RPM	No. of Blades	Blade Setting Angle $\beta_{75\%}$	V_∞ [m/s]	Density [Kg/m ³]	Mach No. M_∞
1	6900	5	69.0°	277.88	0.9488	0.85
2	6000	10	69.0°	263.86	1.0067	0.80
3	6800	10	69.0°	237.13	1.0433	0.70
4	6200	10	69.0°	280.90	0.9151	0.85

Table 5: SR-5 Operating Conditions.

Mach number is about 1.2 at the tip of the blade and the angle of attack at 75% of the span is 8° and 14°, respectively for case 2 and case 3. Figure 17 refers to the operating condition of case 3.

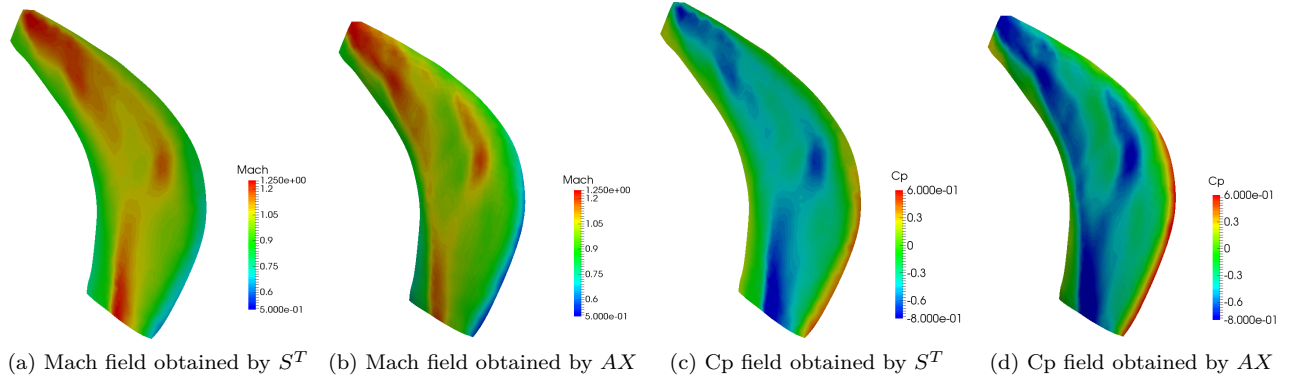


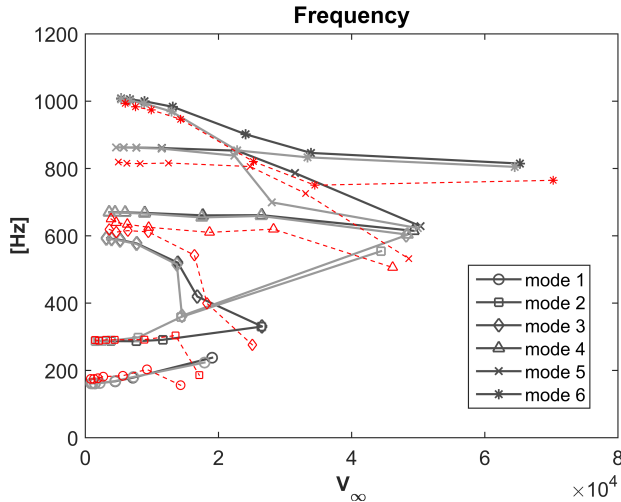
Figure 17: Comparison between Mach and C_p fields.

3 Flutter Analyses

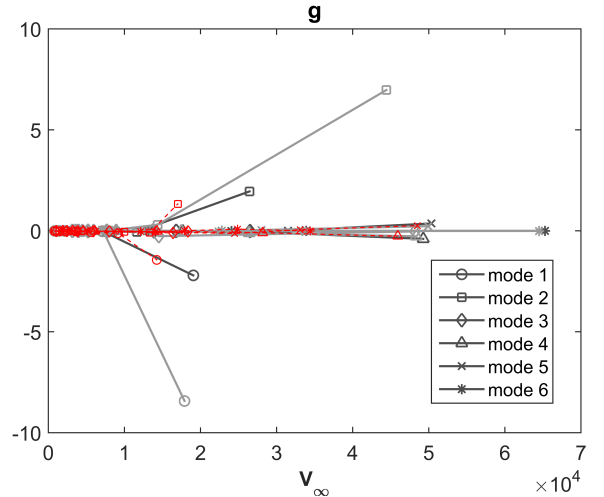
The damping g and the modified eigenvalues ω of the system are calculated for discrete values of reduced frequencies (0.1, 0.2, 0.3, 0.6, 0.9, 1.2, 1.5) using the common K-E method. The aeroelastic system is reduced with the first 6 modes coming from the structural analysis of the blade subjected to centrifugal loads only. It can be inferred that the S^T solver provides results very similar to those obtained in ref.^{25,39} In both cases there is a flutter of the second mode (*i.e.* the second bending one) at the asymptotic velocity of 190 m/s and 179 m/s for case 2 and case 3 respectively and for critical reduced frequencies between 0.2 and 0.3. Looking at $V_\infty - g$ and $V_\infty - \omega$ diagrams, it can be inferred that the flutter instability is a coupled bending-torsion one, because the frequencies of the second and third normal modes tend to get closer. This test case also proves acceptable reliability of the aerodynamic solvers S^T and $AeroX$.

C TEST CASE 3

The blade shape is taken from a US Patent,⁴⁰ which provides the coordinates of various sections of the blade. The blade height is about 1.15 m with a mid chord of 0.4 m. The blade twist and sweep are aerodynamically

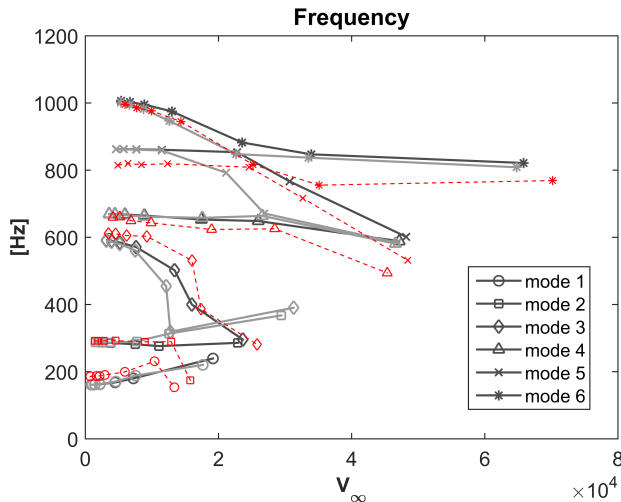


(a) V-f of Case 2.

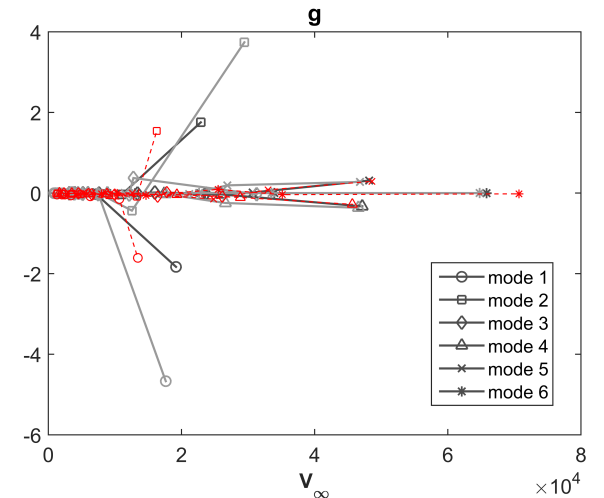


(b) V-g of Case 2.

Figure 18: (●) for S^T , (◐) for *AeroX* and Dashed Line for Reference²⁵.



(a) V-f of Case 3.



(b) V-g of Case 3.

Figure 19: (●) for S^T , (◐) for *AeroX* and Dashed Line for Reference²⁵.

optimized to improve the range of the blade operational flight conditions. Ref.⁴⁰ guarantees no flutter instabilities for a common transport jet flight envelope.

1 Structural Modal Analysis

The blade model is created with two different structural solver (Ansys[®] and NASTRAN[®]). Detailed solid element models with about 30K tetrahedrons have been developed. Table 6 reports the first 6 normal frequencies for an angular velocity of 1900 RPM.

#	type	ANSYS		NASTRAN	
		TET10	TET10	TET10	TET4
1	1st Flap	56.90	57.25	63.46	
2	2nd Flap	127.70	127.92	166.64	
3	1st Tors	195.21	195.54	268.29	
4	3rd Flap	235.41	235.50	344.08	
5	2nd Tors	356.93	357.31	485.72	
6	4th Flap	371.66	371.48	544.99	

Table 6: Rotating Normal Frequencies [Hz] with $\Omega = 1900$ RPM.

2 Aerodynamic Analyses

A trial transport jet is identified for an indicative flutter analyses. To such an aim, the trim condition (Thrust = Drag) is imposed for a steady rectilinear flight at a discrete number of blades pitches and altitudes. At the end of the trim calculations, every selected pitch angle is matched to an asymptotic velocities, V_∞ . As an example, Table 7 reports the relationships between the asymptotic velocities, V_∞ , and the blade pitch angles for the trimmed flight conditions at sea level. Figures 20 and 21 show the Mach and pressure coefficient

Pitch Angle [deg]	45	50	55	60	65	70	75
V_∞ [m/s]	70	90	110	130	150	180	210

Table 7: Relationship between $\beta_{0\%}$ (at the root of the blade) and V_∞ at $h = 0$ m.

fields provided by the full potential scheme S^T and AX Euler solver at two different altitudes. It is worth

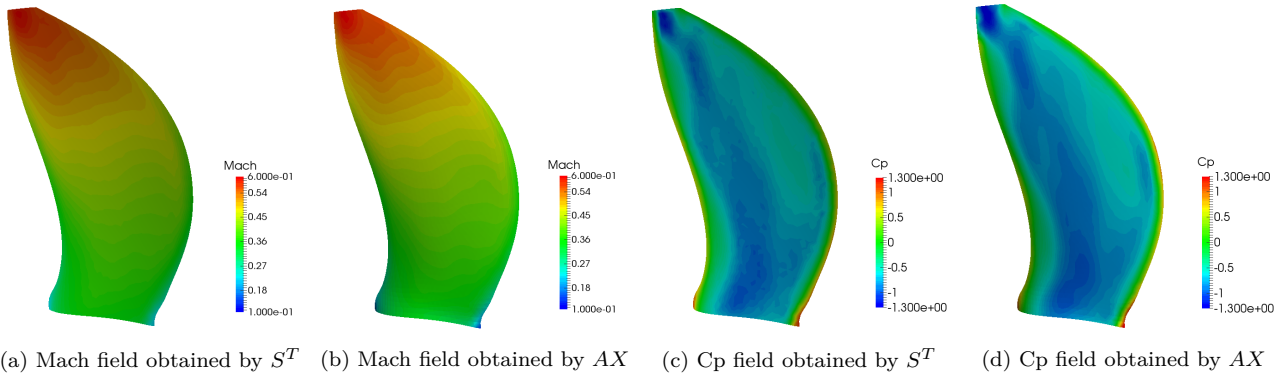


Figure 20: Mach and Cp fields for $V_\infty = 70$ m/s at $h = 0$ m.

noting that the flight conditions are always subsonic except for highest pitch angles (or equivalently the highest trimmed asymptotic velocities V_∞) where the local Mach number can be at most 1.1. Thanks to the "friendly" operating conditions, it is possible to state that the differences between the solutions obtained from S^T and AX are mainly imputable to the different numerical methods implemented.

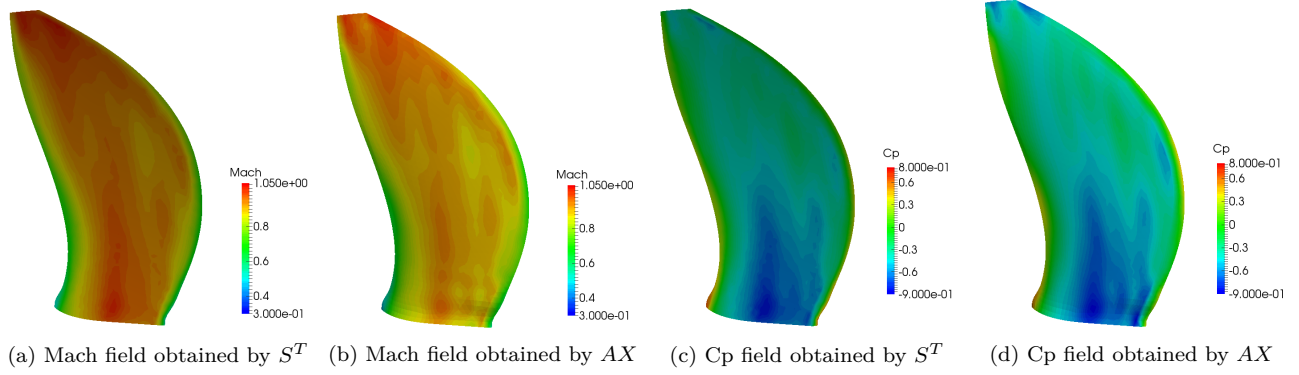


Figure 21: Mach and C_p fields for $V_\infty = 202$ m/s at $h = 10000$ m.

3 Aeroelastic Trim

The static aeroelastic equilibrium has to be computed at every operating flight condition to correctly evaluate the blade deformation, the eigenvalues and the modal shapes. Considering also the aerodynamic load, the aeroelastic equilibrium condition yields to

$$\bar{\mathbf{K}}(\mathbf{q}) \mathbf{q} = \mathbf{F}_C + \mathbf{F}_{\text{aero}}(\mathbf{q}), \quad (19)$$

which is a nonlinear problem that must be solved iteratively. To such an end, the linearization of the steady aerodynamic term of the virtual work, as explained in ref.,⁴¹ is evaluated as

$$\delta W^{\text{aero}} = \delta \mathbf{q}^T \frac{1}{2} \rho V_\infty^2 \int_{\mathcal{S}} \mathbf{X}^T C_p^0 (\vec{n}_0 + \Delta \vec{n}) d\bar{\mathcal{S}}, \quad (20)$$

where $C_p^0 = C_p^0(\mathbf{x}|_{\mathcal{S}}, \bar{t})$ is the steady state pressure coefficient onto the blade surface \mathcal{S} , \vec{n}_0 is the undeformed surface normal and $\Delta \vec{n}$ takes into account the *follower* force contribution. Such term is due to the non-conservative behaviour of the aerodynamic force, which follows the motion of the body surface, being always oriented along its normal. Thus, the term containing $\Delta \vec{n}$ in Eq. 20 provides a follower stiffness matrix, usually called $\mathbf{K}_0^{\text{aero}}$. Eventually, the linearised static aeroelastic trim problem consists in

$$[\bar{\mathbf{K}}(\mathbf{q}_0) + \mathbf{K}_0^{\text{aero}}] \Delta \mathbf{q} = \frac{1}{2} \rho V_\infty^2 \int_{\mathcal{S}} \mathbf{N}^T C_p^0 \vec{n}_0 d\bar{\mathcal{S}}, \quad (21)$$

in which the equilibrium with the centrifugal load is hidden in $\bar{\mathbf{K}}(\mathbf{q}_0)$. After computing the right hand side of Eq. 21, a new eigenvalue problem is solved. In this case, it is demonstrated that the effects of the aerodynamic loads are negligible with respect to those associated to the centrifugal forces, so it is not required to perform the static aeroelastic equilibrium for every flight condition. Table 8 reports the first 6 normal frequencies calculated for a blade pitch angle of 75° at a flight velocity $V_\infty = 210$ m/s and at an angular velocity of 895 RPM.

In addition, it can be inferred that the new equilibrium condition coming from Eq. 21 is very similar to that of the centrifugal equilibrium (the differences of the displacement fields of these two equilibrium solutions

<i>type</i>	1st Flap	2nd Flap	1st Tors	3rd Flap	2nd Tors	4th Flap
Cent+Aero	49.13	116.98	182.59	222.28	345.24	357.04
Cent	49.09	116.85	182.49	222.02	345.26	356.67

Table 8: Comparing Normal Frequencies [Hz] with or without the aerodynamic pressure load.

is less than 2%), so to prove that the contribution of the matrix $\mathbf{K}_0^{\text{aero}}$ is negligible also for updating the blade deformed shape and not only for the eigensolution of such system. In conclusion, this analysis proves that the equilibrium condition is predominantly affected by the centrifugal loading, so the static aeroelastic trim can be avoided because the aerodynamic loads do not have a strong influence on the eigenvalues, mode shape and deformed configuration of the blades. Such an approach justifies the mostly adopted way in the literature.

4 Flutter Analyses

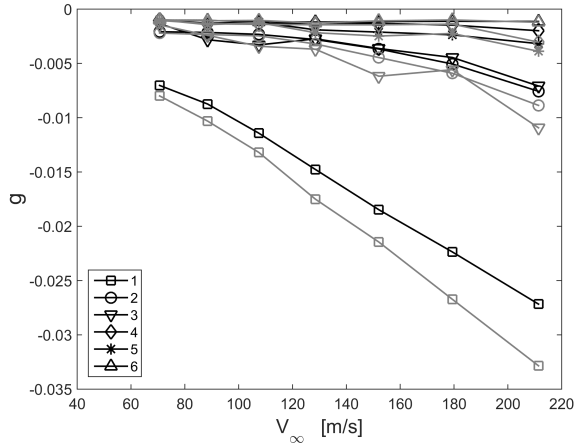
The GAFs are calculated for each trimmed flight condition and for every altitude considered. After performing a parametric stability analysis of the linear(ized) aeroelastic time-invariant system it is possible to build the $V_\infty - \omega$ and $V_\infty - g$ diagrams shown in Figure 22. The flutter boundaries are investigated at different altitudes so verifying the critical conditions in a representative flight envelope of a common jet transport aircraft. In agreement with ref.⁴⁰ there are no classical flutter instabilities for this aeroelastically optimized blade. The values of the damping g obtained with the FP code S^T are more conservative than those obtained with the Euler solver AX . It can also be observed that the values of g are lower than those of common wing test cases, *e.g.* ref.⁴² and was already justified by ref.²⁹ and ref.[?] It can be inferred that the centrifugal force has greater importance than the aerodynamic load, so the effects of the latter have less influence on the (in)stability of the system.

D TEST CASE 4

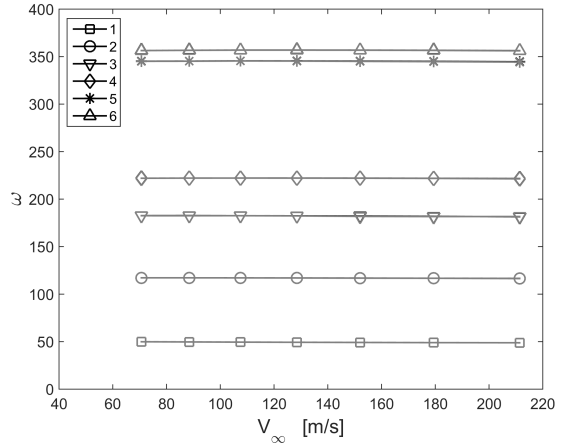
After demonstrating the capabilities of the S^T solver, a flutter analysis of a CRP has been carried out. The blade shape is the same as the previous test case (ref.⁴⁰). The analyzed CRP is composed of two 8-bladed stages placed at a distance of $d/D = 0.25$, in accordance to the guidelines explained in ref.⁶ and ref.⁷. The internal radius is $r = 0.76$ m and the disk diameter is $D = 3.7041$ m. The aerodynamic meshes and the flight conditions are the same as those in Section C.

1 Aerodynamic Analyses

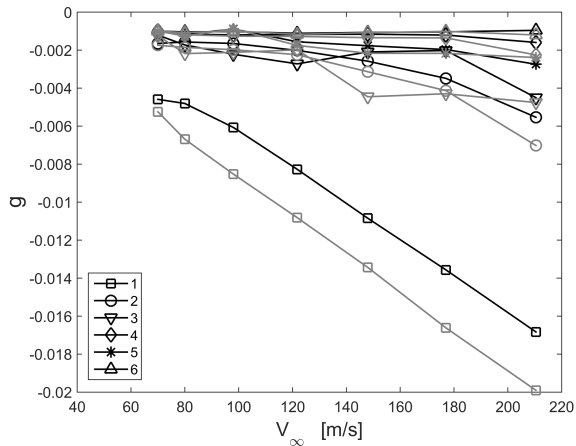
First, the assumption of equally partitioned thrust between both rotors at each asymptotic velocity V_∞ must be set adjusting the blade pitches by means of the transpiration boundary conditions. In every case, the



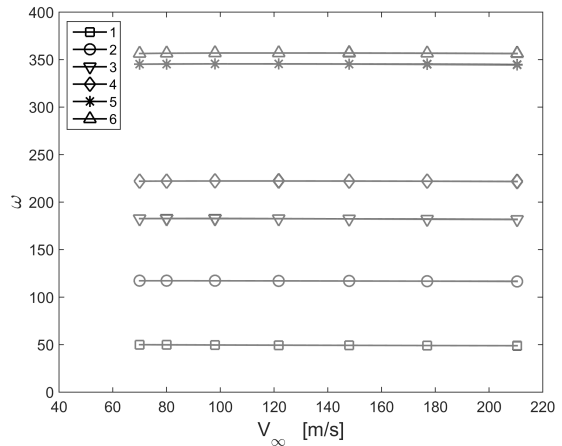
(a) $V_\infty - g$ diagram at 0 m.



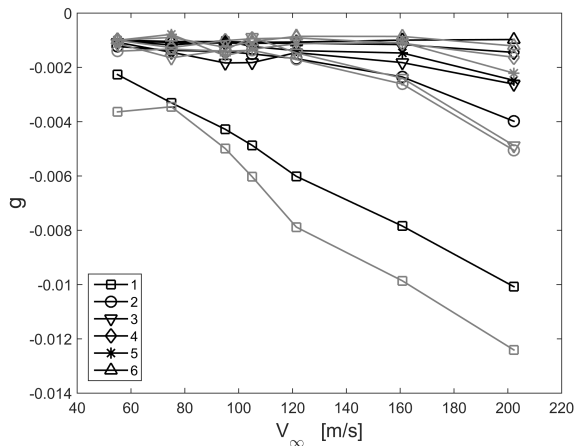
(b) $V_\infty - \omega$ diagram at 0 m.



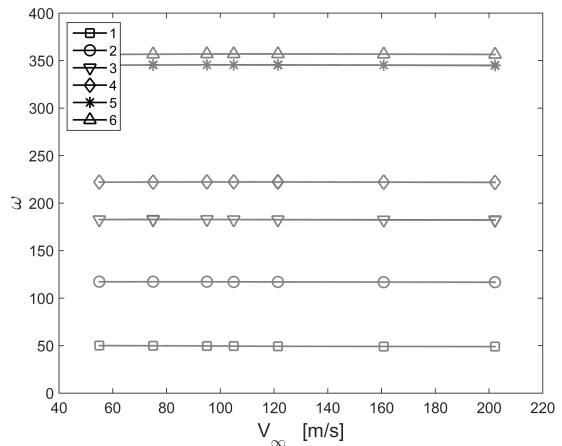
(c) $V_\infty - g$ diagram at 5000 m.



(d) $V_\infty - \omega$ diagram at 5000 m.



(e) $V_\infty - g$ diagram at 10000 m.



(f) $V_\infty - \omega$ diagram at 10000 m.

Figure 22: Flutter results for test case 3. The legends refer to the modes numbers of Table 6.

pitch angles of the blades of the front and after rotor are modified by about two degrees at most with respect to the values related to the SRP case (see Table 9).

V_∞ [m/s]	70.0	90.0	110.0	130.0	150.0	180.0	210.0
SRP $\beta_{0\%}$ [deg]	45.0	50.0	55.0	60.0	65.0	70.0	75.0
Front Rotor $\beta_{0\%}$ [deg]	44.9	50.0	55.0	60.0	65.0	71.1	77.5
After Rotor $\beta_{0\%}$ [deg]	44.8	50.1	55.5	60.7	66.3	71.3	76.5

Table 9: Pitch Angles $\beta_{0\%}$ for CRP.

2 Flutter Analyses

The flutter analysis is carried out only at sea level. As already explained in Section IV, different results can be obtained in relation with the beginning of the blended step input in the oscillation period of the aerodynamic load. The transient of such input must be lesser than one period so simulating nearly a step. In particular, the chosen transient lasts about an half of a period. In this way, the assumption of a "frozen" stability analysis is valid because the change of the aerodynamic boundary conditions is very fast. Thus, the results are obtained for two different beginnings of the input, at $\Phi = 0^\circ$ and $\Phi = 180^\circ$. In other words, $\Phi = 0^\circ$ means that the input starts at the beginning of the oscillating period while $\Phi = 180^\circ$ means the half of the oscillating period. The assumption of a *small varying system* is legitimated by the small variation of the aerodynamic loads as shown in Figure 16. The results are reported in Figures 23 and 24. They cannot be verified since no corresponding analyses has been found in the literature. It can be noted that the third mode (torsional) of the rear rotor assumes positive values of the damping g . In particular, the flutter velocities are $V_f = 212$ m/s and $V_f = 202$ m/s for $\Phi = 0^\circ$ and $\Phi = 180^\circ$, respectively.

VI Concluding Remarks

The effectiveness of the proposed aeroelastic analyses has been successfully assessed by tackling a set of realistic dynamic problems and by comparing the results with reference experimental and numerical data available in the literature and with the Euler flow solver *AeroX* simulations (ref.^{31,32}). In particular, the capabilities of the FP aerodynamic solver S^T (ref.^{10,11}) are pointed out comparing the results obtained from uRANS and Euler simulations of ref.⁷ A good accordance with uRANS simulations is obtained even if local Mach numbers reach high transonic values. It is also shown that the *ad hoc* technique for computing the flow field around CRP provides fair correlations against more sophisticated strategies, *e.g.* Chimera method. The blade pitch angles obtained for an equally partitioned thrust between the two rotor are in accordance to those obtained by ref.⁷. Thus, the transpiration technique can be an effective tool not only for simulating the generalized aerodynamic forces $Q_a(t)$ but also for varying the blade pitch. The flutter stability of CRPs

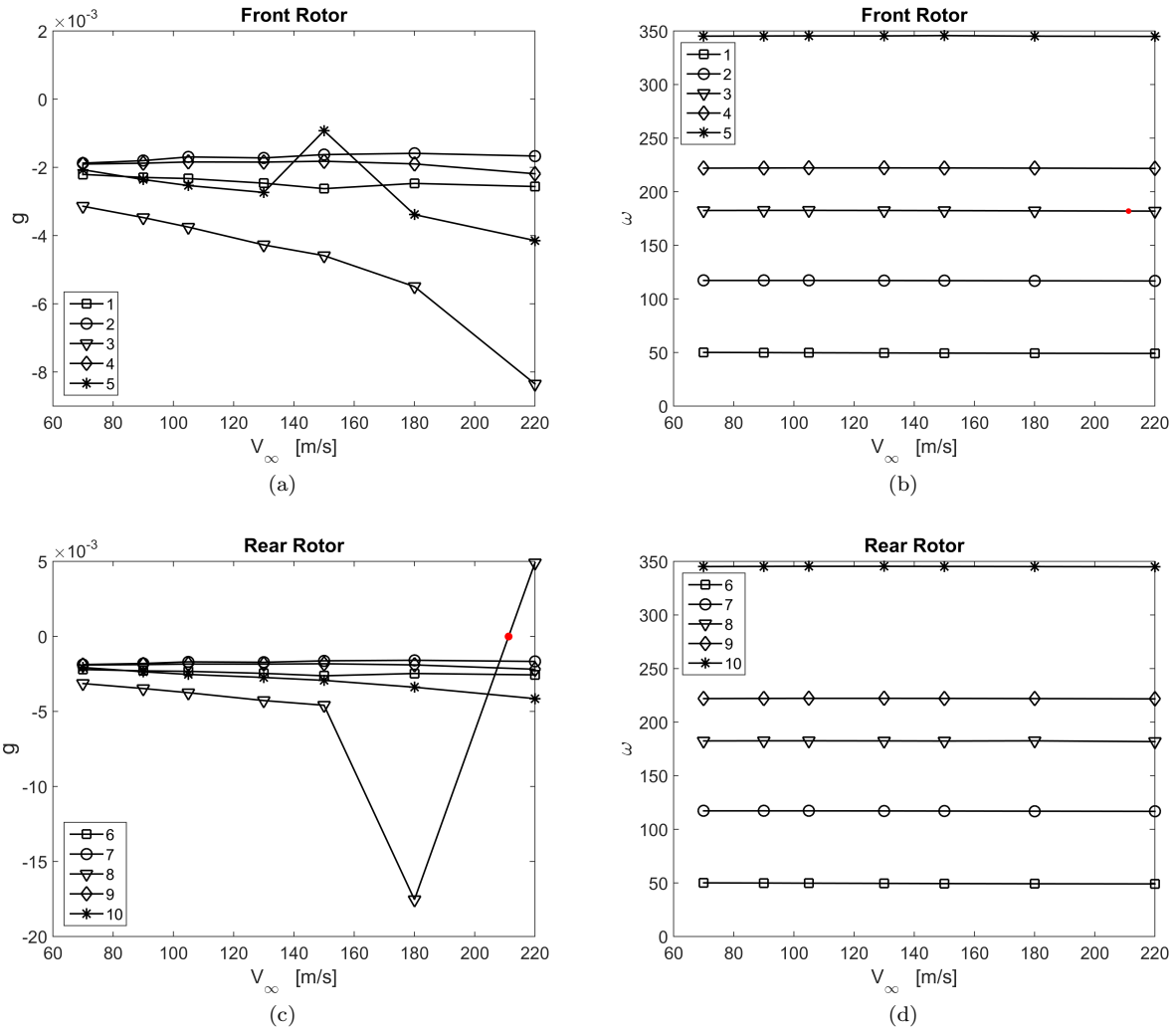


Figure 23: $V_\infty - g$ and $V_\infty - \omega$ with $\Phi = 0^\circ$. The legends refer to the modes numbers of Table 6.

has been investigated on the base of justified assumptions related to the resources available for the present work. Such a system, which responses are time-periodic, can be considered as a small-varying system so enabling a *frozen* stability analysis. Two complete studies of the patent blade of ref.⁴⁰ are surveyed with the awareness gained by the previous validation process. The static aeroelastic trim analysis conducted for this blade proves that the effects of the aerodynamics loads are negligible with respect to those of the centrifugal force in terms of eigenvalues, mode shapes and deformed configurations. Thus, such analysis can be avoided, so proving that trimmed conditions based on centrifugal load only are quite acceptable as it is usually assumed in the literature. The flutter boundaries of both SRPs and CRPs are evaluated in a plausible flight envelope by taking trimmed flight conditions of a typical jet transport aircraft. The stability of the SRP is verified to be in accordance with what stated in the patent. The damping values g are always smaller with respect to those of common wings. Such a fact is well documented in the literature; so other

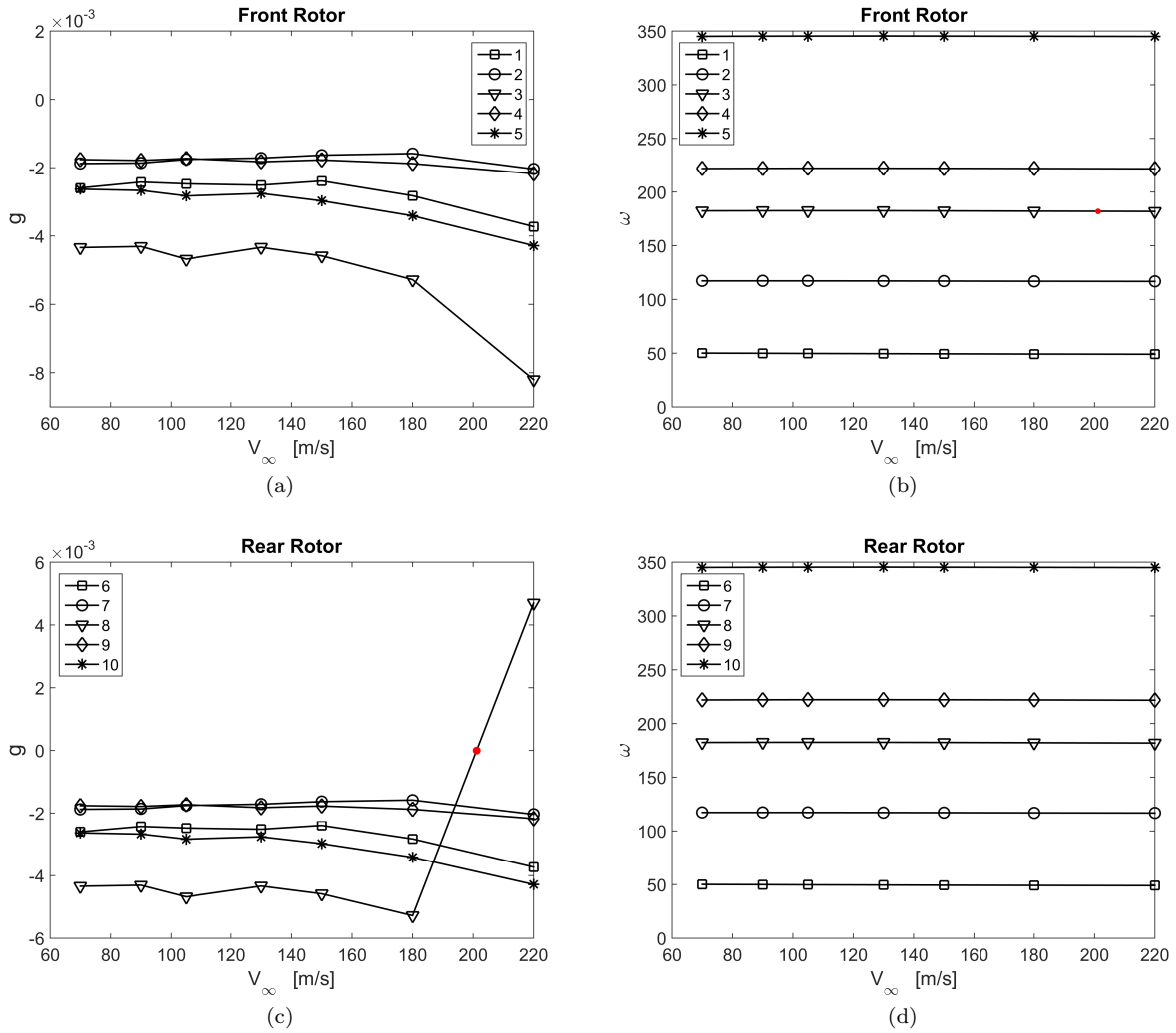


Figure 24: $V_\infty - g$ and $V_\infty - \omega$ with $\Phi = 180^\circ$. The legends refer to the modes numbers of Table 6.

forms of damping are needed to augment the stability region of such systems.

References

- ¹Lambert, C., "Aviation and Environment - Open Rotor Engines," *SBAC, Aviation and Environment Briefing Papers*, 2012.
- ²Stuermer, A. and Yin, J., "Aerodynamic and aeroacoustic installation effects for pusher-configuration CROR propulsion systems," *28th AIAA Applied Aerodynamics Conference Chicago, Illinois*, AIAA journal, 2010.
- ³Middleton, P., "Frugal, fast, but fractious prop-fan technology," *Flight International*, Vol. 126, 1984, pp. 113–116.
- ⁴Hager, R. and Vrabel, D., "Advanced turboprop project," Tech. Rep. NASA-SP-495, NASA, Lewis Research Center, 1988.
- ⁵Vernon, D., Page, G., and Welge, H., "Propfan experimental data analysis," Tech. rep., NASA.
- ⁶Sullivan, W., Turnberg, J., and Violette, J., "Large-scale Advanced Prop-fan (LAP) Blade Design," Tech. rep., NASA,

1984.

⁷Stuermer, A., “Unsteady CFD Simulations of Contra-Rotating Propeller Propulsion Systems,” *44th AIAA/ASME/SAE/ASEE Joint Propulsion Conference & Exhibit Hartford, CT*, AIAA journal, 2008.

⁸Bakhle, M., Keith, T., and Williams, M., “Unsteady aerodynamics and flutter based on the potential equation,” *29th Joint Propulsion Conference and Exhibit*, AIAA journal, 1993.

⁹Ku, C. and Williams, M., “Three dimensional full potential method for the aeroelastic modeling of propfans,” *31st Structures, Structural Dynamics and Materials Conference Long Beach, CA*, AIAA journal, 1990.

¹⁰Parrinello, A. and Mantegazza, P., “Independent Two-Fields Solution for Full-Potential Unsteady Transonic Flows,” *AIAA journal*, Vol. 48, No. 7, 2010, pp. 1391–1402.

¹¹Parrinello, A. and Mantegazza, P., “Improvements and Extensions to a Full-Potential Formulation Based on Independent Fields,” *AIAA journal*, Vol. 50, No. 3, 2012, pp. 571–580.

¹²Hirsch, C., *Numerical Computation of Internal and External Flows: The Fundamentals of Computational Fluid Dynamics*, Vol. 1, Butterworth-Heinemann, 2007, pages 54–57.

¹³Donea, J., Giuliani, S., and Halleux, J.-P., “An arbitrary Lagrangian-Eulerian finite element method for transient dynamic fluid-structure interactions,” *Computer methods in applied mechanics and engineering*, Vol. 33, No. 1-3, 1982, pp. 689–723.

¹⁴Chesshire, G. and Henshaw, W., “Composite overlapping meshes for the solution of partial differential equations,” *Journal of Computational Physics*, Vol. 90, 1990, pp. 1–64.

¹⁵Biedron, R. and Thomas, J., “Recent enhancements to the fun3d flow solver for moving-mesh applications,” *AIAA Paper*, Vol. 1360, 2009, pp. 2009.

¹⁶Geradin, M. and Kill, N., “A new approach to finite element modelling of flexible rotors,” *Engineering Computations*, Vol. 1, No. 1, 1984, pp. 52–64.

¹⁷Gans, H., *Structural optimization including centrifugal and Coriolis effects*, Ph.D. thesis, Air Force Institute of Technology, 1988.

¹⁸Bathe, K., *Finite Element Procedures*, Prentice-Hall International Series in, Prentice Hall, 1996, Chapter 4, pages 148–168.

¹⁹Software, M., “MSC/NASTRAN Advanced Analysis User Guide,” 2010.

²⁰Fluent, “14.0 User’s Manual,” *ANSYS Inc., Canonsburg, PA*, 2011.

²¹Yang, H., *3D unsteady flow in oscillating compressor cascade*, Ph.D. thesis, Durham University, 2004.

²²Lane, F., “System mode shapes in the flutter of compressor blade rows,” *Journal of the Aeronautical Sciences*, Vol. 23, No. 1, 1956, pp. 54–66.

²³Donini, N., *Aeroelasticity of turbomachines linearized flutter analysis*, Master’s thesis, Politecnico di Milano, 2012.

²⁴Hassig, H., “An approximate true damping solution of the flutter equation by determinant iteration,” *Journal of Aircraft*, Vol. 8, No. 11, 1971, pp. 885–889.

²⁵Elchuri, V. and Smith, G., “Flutter analysis of advanced turbopropellers,” *AIAA journal*, Vol. 22, No. 6, 1984.

²⁶Mantegazza, P. and Cardani, C., “An iterative technique to compute flutter speed through the simultaneous solution of each aeroelastic mode and frequency at increasing speed,” *Aerotecnica Missili Spazio*, Vol. 54, 1975, pp. 286–291.

²⁷Mantegazza, P. and Cardani, C., “Continuation and direct solution of the flutter equation,” *Computers & Structures*, Vol. 8, No. 2, 1978, pp. 185–192.

²⁸Roskam, J., *Airplane Design: Determination of stability, control, and performance characteristics, FAR and military requirements*, DAR corporation, 1985, Part VI (Chapter 4).

²⁹August, R., “Vibration and flutter analysis of the SR-7L large-scale propfan,” Tech. rep., NASA, 1988, pages 8–9.

- ³⁰Vidyasagar, M., *Nonlinear systems analysis*, Prentice Hall, 1993, Chapter 6, pages 337–365.
- ³¹Mangani, L., Romanelli, G., Gadda, A., and Casartelli, E., “Comparison of acceleration techniques on CFD open-source software for aerospace applications,” *AIAA journal*, 2015.
- ³²Romanelli, G., Mangani, L., Casartelli, E., Gadda, A., and Favale, M., “Implementation of an explicit density-based unstructured CFD solver for turbomachinery applications on graphical processing units,” *ASME paper*, 2015.
- ³³Parrinello, A., Morandini, M., and Mantegazza, P., “Automatic Embedding of Potential Flow Wake Surfaces in Generic Monolithic Unstructured Meshes,” *Journal of Aircraft*, Vol. 50, No. 4, 2013, pp. 1179–1188.
- ³⁴Gerhold, T., “Overview of the hybrid RANS code TAU,” *MEGAFLOW-Numerical Flow Simulation for Aircraft Design*, Springer, 2005, pp. 81–92.
- ³⁵Madrane, A., Raichle, A., and Stuermer, A., “Parallel Implementation of a Dynamic Unstructured Chimera Method in the DLR Finite Volume TAU-code,” *12th Annual Conference of the CFD Society of Canada*, 2004.
- ³⁶Elchuri, V., Gallo, A., and Skalski, S., “NASTRAN documentation for flutter analysis of advanced turbopropellers,” Tech. rep., NASA, 1982.
- ³⁷Elchuri, V. and Smith, G., “NASTRAN flutter analysis of advanced turbopropellers,” Tech. rep., NASA, 1982.
- ³⁸Zucchi, M., *Problemi aeroelastici dei propfan*, Master’s thesis, Politecnico di Milano, 1986.
- ³⁹Narayanan, G. V. and Kaza, K., “ASTROP2 users manual: a program for aeroelastic stability analysis of propfans,” Tech. rep., NASA, 1991.
- ⁴⁰Rothman, E. and Violette, J., “Prop-fan with improved stability,” *US 4730985*, Google Patents, 1988.
- ⁴¹Bisplinghoff, R., Ashley, H., and Halfman, R., *Aeroelasticity*, Courier Corporation, 2013.
- ⁴²Yates, J. and Carson, E., “AGARD standard aeroelastic configurations for dynamic response of wing 445.6,” Tech. Rep. NASA-TM-100492, NASA, 1988.